Received: 8 February 2020 | Revised: 21 July 2020 | Accepted: 19 August 2020

DOI: 10.1002/nag.3140



WILEY

RESEARCH ARTICLE

# Anisotropic dual-continuum representations for multiscale poroelastic materials: Development and numerical modelling

**Mark Ashworth** | **Florian Doster**

Institute of GeoEnergy Engineering, Heriot-Watt Unversity, Edinburgh, U.K, EH14 4AP

**Correspondence**
Mark Ashworth, Institute of GeoEnergy Engineering, Heriot-Watt University, EH14 4AP Edinburgh, U.K.
Email: ma174@hw.ac.uk

**Funding information**
Natural Environmental Research Council

**Summary**

Dual-continuum (DC) models can be tractable alternatives to explicit approaches for the numerical modelling of multiscale materials with multiphysics behaviours. This work concerns the conceptual and numerical modelling of poroelastically coupled dual-scale materials such as naturally fractured rock. Apart from a few exceptions, previous poroelastic DC models have assumed isotropy of the constituents and the dual-material. Additionally, it is common to assume that only one continuum has intrinsic stiffness properties. Finally, little has been done into validating whether the DC paradigm can capture the global poroelastic behaviours of explicit numerical representations at the DC modelling scale. We address the aforementioned knowledge gaps in two steps. First, we utilise a homogenisation approach based on Levin's theorem to develop a previously derived anisotropic poroelastic constitutive model. Our development incorporates anisotropic intrinsic stiffness properties of both continua. This addition is in analogy to anisotropic fractured rock masses with stiff fractures. Second, we perform numerical modelling to test the DC model against fine-scale explicit equivalents. In doing, we present our hybrid numerical framework, as well as the conditions required for interpretation of the numerical results. The tests themselves progress from materials with isotropic to anisotropic mechanical and flow properties. The fine-scale simulations show that anisotropy can have noticeable effects on deformation and flow behaviour. However, our numerical experiments show that the DC approach can capture the global poroelastic behaviours of both isotropic and anisotropic fine-scale representations.

**KEYWORDS**

anisotropy, constitutive modelling, dual-continuum, homogenisation, hybrid numerical framework, poroelasticity

## 1 | INTRODUCTION

Numerical modelling of multiscale, poroelastically coupled materials can be challenging due to inherent length scale heterogeneities and multiphysics behaviours. Explicit modelling approaches allow one to account for each length scale

directly within a model. This representation can therefore provide accurate and detailed descriptions. However, the number of degrees of freedom needed for direct models of multiscale, poroelastic materials can make simulation computationally prohibitive. Further, particularly within the subsurface, the data needed to populate such explicit approaches may be sparse.

Implicit models alleviate the problems associated with explicit models, at the expense of abstraction of local-scale physics. One such modelling concept is the dual-continuum (DC) model, originally attributed to Barenblatt et al.[1] This implicit approach has been used successfully within the context of flow modelling in a variety of subsurface engineering settings.[2-5] In the DC paradigm, one continuum represents a high-storage, low-permeability material (e.g., matrix), whilst the other represents a low-storage, high-permeability material (e.g., fractures).

This work concerns the DC modelling of multiscale, poroelastic geomaterials. We address two knowledge gaps associated with the DC modelling paradigm within the context of poroelasticity as follws:

First, we develop the poroelastic DC modelling approach. We introduce the underlying modelling assumptions whilst considering the material symmetry and mechanical properties of the constituents in the process. With respect to the latter, previous poroelastic DC models have, for the most part, assumed isotropy of the continua and bulk material.[6-9] However, rock formations are well known to exhibit anisotropic properties.[10-12] Recent work by Zhang et al[13] showed that anistotropic permeabilities can have measurable impacts on the flow patterns in poroelastic DC materials. Further to anisotropy, and in the case of fractured materials, the fractures themselves can have intrinsic mechanical properties owing to local asperities and/or bridging material between fracture faces.[14-16] Intrinsic mechanical properties of both continua have been considered for isotropic materials in the works of Berryman,[17,18] Elsworth and Bai[19] and Nguyen and Abousleiman.[20] In this work, we further explore the impact of the anisotropic elasticity, in addition to permeabilities, on DC responses.

Incorporating anisotropic and intrinsic properties can be done at the constitutive modelling stage. In the following, we add to a micromechanically derived anisotropic constitutive model by Dormieux et al.[21] Contrary to the model by Dormieux et al,[21] we incorporate linear (poro-)elastic properties for the low-storage, high-permeability continuum at the microscale. In this case, *both* continua have intrinsic stiffness properties. Following homogenisation, the resulting model, complete with expressions for the effective parameters, is an anisotropic, dual-stiffness constitutive model. Previous isotropic constitutive models reviewed in Ashworth and Doster[22] can then be recovered under isotropy and void-space assumptions on the general anisotropic, dual-stiffness constitutive model derived herein.

Second, with the derived poroelastic constitutive model, we proceed to numerical modelling. We investigate whether the DC representation is able to capture the global poroelastic behaviours of a fine-scale (FS) explicit model at the DC modelling scale. Whilst work has gone into testing and validating the DC concept for the flow problem (e.g., previous studies[23,24]), little has been done to asses validity of the poroelastically coupled DC approach. Further, we discuss several considerations to ensure meaningful interpretations between the two modelling approaches.

To summarise, our aims are twofold. First, in Section 2, we use a homogenisation approach and develop a previously introduced anisotropic DC constitutive model. For this development, we allow both continua to have (anisotropic) intrinsic mechanical properties. Second, we perform numerical modelling of the poroelastic DC concept, investigating its validity against FS explicit representations. To do so, we introduce the hybrid numerical framework used to perform the numerical study in Section 3. We present the numerical tests, modelling considerations and test results in Section 4. For our study, we consider numerical test cases as conceptualisations of naturally fractured rock samples that satisfy certain representative elementary volume (REV) requirements. Our results show that the DC model is capable of capturing the global poroelastic behaviours of isotropic and anisotropic FS equivalents. Finally, we offer conclusions and recommendations for future work in Section 5.

## 2 | HOMOGENISATION OF THE DUAL PROBLEM

In the following, we develop the anisotropic, dual-stiffness constitutive model for a poroelastic DC material. To do so, we expand the homogenisation approach originally proposed by Dormieux et al[21] by including intrinsic mechanical properties for the low-storage, high-permeability continuum.

Whilst this work strictly assumes linear poroelasticity, the inclusion of stiffness properties are necessary for extensions to nonlinear modelling of materials.[25] For example, it is well known that mechanically weak materials, such as fractures, show nonlinearly elastic, or inelastic, hardening behaviours even at small deformations.[15,26-28] We

acknowledge the simplifying assumptions used in the current work, with a view to incorporating more realistic deformation behaviours on the basis of the modelling concepts developed herein.

To keep notation brief, we refer to the low-permeability storage continuum as the *matrix* continuum and the low-storage, high-permeability transport continuum as the *fracture* continuum. However, this work is sufficiently general such that other multiscale materials can be considered, for example, soil aggregates (under the assumption of infinitesimal deformations).[7,29]

## 2.1 | Volume averaging

We define the averaging operation, and assumptions therein, required in the homogenisation approach. A DC representation can be justified if an REV can be taken from a large macroscopic structure. Identification of an REV requires the satisfaction of the scale separation principle summarised as[30]

$$s \ll S \ll L, \tag{1}$$

where $s$, $S$ and $L$ denote the characteristic lengths at the local heterogeneity, REV and macroscopic body scales, respectively. Equation (1) should honour length scale requirements for the physical system, both geometrically (Figure 1), and with respect to the wavelengths of the physical process.[31,32] Accordingly, the REV represents the scale at which relationships between averaged quantities are defined (Figure 1).

Defining an REV over fractured media is a subject of much debate due to the challenge of establishing criteria for scale separation.[33-36] In the following, however, we suppose a material for which an REV can be defined, such as densely fractured rock masses.[37]

To proceed, we assume statistical homogeneity of the underlying material and thus make use of the volume average over the REV[38]

$$\overline{\boldsymbol{z}} = \frac{1}{|\Omega|}\int_{\Omega} \boldsymbol{z}(\boldsymbol{x})\, dV, \tag{2}$$

where $\boldsymbol{z}$ is an arbitrary tensor field, $\boldsymbol{x}$ is the microscopic position vector within an REV and $|\Omega|$ is the volume of the REV within the body.

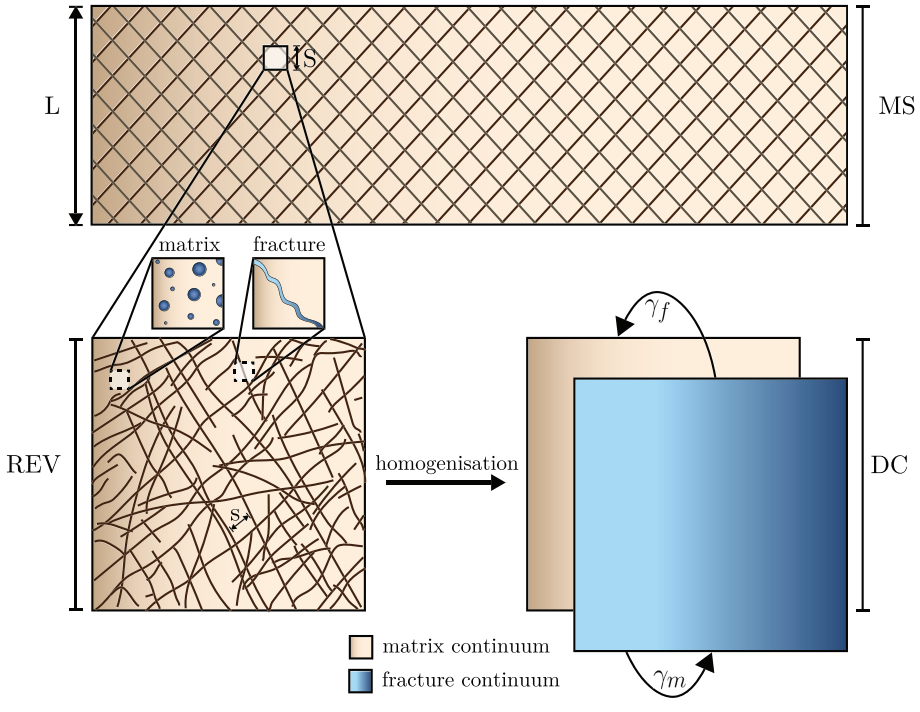


**FIGURE 1** A geometrical interpretation of an representative elementary volume (REV) over a microscopic scale from a large macroscopic structure (MS). The REV is used to define the macroscopic dual-continuum (DC) model in which matrix ($m$) and fracture continua ($f$) are superposed in space and time. Intercontinuum mass exchange is described by the transfer term $\gamma_\alpha$ [$\alpha = m,f$]. Notations $s$, $S$ and $L$ denote characteristic lengths of local heterogeneities, the REV and the macroscopic structure, respectively [Colour figure can be viewed at wileyonlinelibrary.com]

## 2.2 | Homogenisation

### 2.2.1 | Preliminaries

To develop the homogenisation problem introduced by Dormieux et al,[21] we consider the domain, $\Omega$, over an REV in which there exists a porous matrix continuum, $\Omega_m \subset \Omega$, and porous fracture continuum, $\Omega_f \subset \Omega$. We assume linear poroelasticity for each continuum[39,40] and that the continua are saturated by the same slightly compressible fluid. Further, we assume isothermal evolutions and zero initial stress and pressure conditions.

An important assumption is that we consider microscopic fluctuations in pressures are negligible with respect to the macroscopic (average) continuum pressures.[21] As a result, fluids are assumed to be in steady state, but at different equilibrium pressures, within the respective continua in the REV. Accordingly, we model solid-fluid interactions at the microscale using uniform continuum pressures.[41]

With the given assumptions, the local constitutive model for a continuum, $\alpha$, is then

$$\sigma_\alpha = \mathbb{C}_\alpha : \boldsymbol{\epsilon}_\alpha - \boldsymbol{b}_\alpha P_\alpha \text{ in } \Omega_\alpha, \tag{3}$$

$$\mathrm{d}\varphi_\alpha = \boldsymbol{b}_\alpha : \boldsymbol{\epsilon}_\alpha + \frac{1}{n_\alpha} P_\alpha \text{ in } \Omega_\alpha, \tag{4}$$

where $\mathbb{C}_\alpha$ $[\alpha = m,f]$ is the intrinsic fourth-order stiffness tensor for continuum $\alpha$ and the second-order tensors, $\boldsymbol{\sigma}_\alpha$, $\boldsymbol{\epsilon}_\alpha$, $\boldsymbol{b}_\alpha$, are the microscopic Cauchy stress and linearised strain tensors and intrinsic Biot coefficient for continuum $\alpha$, respectively. Parameter $n_\alpha^{-1}$ is the inverse of the Biot modulus, $P_\alpha$ is the macroscopic fluid pressure and $\mathrm{d}\varphi_\alpha = \varphi_\alpha - \varphi_\alpha^0$ is the evolution of the local Lagrangian porosity from the reference state (denoted by superscript 0), all written in terms of continuum $\alpha$. The local Lagrangian porosity is the ratio of the continuum pore volume, $|\Omega_\alpha^p|$, to the bulk volume of the undeformed continuum configuration, $|\Omega_\alpha^0|$. As is customary, we take stress and strain as positive in the tensile direction.

It is useful to rewrite Equations (3) to (4) in a unified way as follows:[21]

$$\sigma(\boldsymbol{x}) = \mathbb{C}(\boldsymbol{x}) : \boldsymbol{\epsilon}(\boldsymbol{x}) + \sigma^p(\boldsymbol{x}) \; \forall \boldsymbol{x} \in \Omega, \tag{5}$$

where $\mathbb{C}(\boldsymbol{x})$, and the prestress tensor distributions related to the fluid pressure,[42] $\boldsymbol{\sigma}^p(\boldsymbol{x})$, are given by

$$\mathbb{C}(\boldsymbol{x}) = \begin{cases} \mathbb{C}_m & \text{in } \Omega_m \\ \mathbb{C}_f & \text{in } \Omega_f \end{cases}, \tag{6}$$

$$\sigma^p(\boldsymbol{x}) = \begin{cases} -\boldsymbol{b}_m P_m & \text{in } \Omega_m \\ -\boldsymbol{b}_f P_f & \text{in } \Omega_f \end{cases}, \tag{7}$$

respectively.

The essence of the homogenisation approach is to define a boundary value problem on the REV, the solution to which allows for the determination of macroscopic constitutive properties. Accordingly, the conservation of momentum boundary value problem is defined as

$$\nabla \cdot \sigma = 0 \text{ in } \Omega, \tag{8}$$

$$\sigma = \mathbb{C}(\boldsymbol{x}) : \boldsymbol{\epsilon} + \sigma^p(\boldsymbol{x}) \text{ in } \Omega, \tag{9}$$

$$\hat{\boldsymbol{u}} = \mathbf{E} \cdot \boldsymbol{x} \text{ on } \partial\Omega, \tag{10}$$

where $\partial\Omega$ is the boundary of $\Omega$, $\boldsymbol{u}$ is the microscopic displacement vector and $\mathbf{E}$ is the macroscopic (or surface prescribed) strain tensor. Quantities denoted by $\hat{}$ are boundary assigned values, that is, $\boldsymbol{u} = \hat{\boldsymbol{u}}$ on $\partial\Omega$.

Using the averaging operation, Equation (2), it can be shown (e.g., Hashin[43]) for uniform displacement boundary conditions, Equation (10), that

$$\mathbf{E} = \overline{\boldsymbol{\epsilon}} \tag{11}$$

and

$$\overline{\boldsymbol{\epsilon}} = v_m \overline{\boldsymbol{\epsilon}}_m + v_f \overline{\boldsymbol{\epsilon}}_f, \tag{12}$$

where $\overline{\boldsymbol{z}}_\alpha = |\Omega_\alpha|^{-1} \int_{\Omega_\alpha} \boldsymbol{z}_\alpha(\boldsymbol{x}) dV$ and $v_\alpha$ is the volume fraction of continuum $\alpha$, defined as the ratio of the continuum volume, $|\Omega_\alpha^0|$, to the bulk volume, $|\Omega^0|$, taken at reference conditions.

To give the link between microscopic fields, in this case strain, and macroscopic counterparts, we consider a mapping between $\epsilon(\boldsymbol{x})$ and $\mathbf{E}$. Owing to the linearity of Equation (8), we can define a linear mapping so that

$$\boldsymbol{\epsilon}(\boldsymbol{x}) = \mathbb{A}(\boldsymbol{x}) : \mathbf{E}, \tag{13}$$

where $\mathbb{A}(\boldsymbol{x})$ is the fourth-order mapping tensor.[44]

Finally, combining Equations (11) to (13), it can be shown that

$$\overline{\boldsymbol{\epsilon}} = v_m \overline{\mathbb{A}}_m : \mathbf{E} + v_f \overline{\mathbb{A}}_f : \mathbf{E}, \tag{14}$$

from which we can see

$$\mathbb{I} = \overline{\mathbb{A}} = v_m \overline{\mathbb{A}}_m + v_f \overline{\mathbb{A}}_f, \tag{15}$$

where $\mathbb{I}$ is the fourth-order identity tensor.

### 2.2.2 | Recovery of the constitutive system

From the superposition property in linear systems, Equations (8) to (10) can be decomposed into two subproblems. Subproblem I can be interpreted as a drained poroelastic problem as follows:

$$\nabla \cdot \boldsymbol{\sigma}^{\mathrm{I}} = 0 \text{ in } \Omega, \tag{16}$$

$$\boldsymbol{\sigma}^{\mathrm{I}} = \mathbb{C}(\boldsymbol{x}) : \boldsymbol{\epsilon}^{\mathrm{I}} \text{ in } \Omega, \tag{17}$$

$$\hat{\boldsymbol{u}}^{\mathrm{I}} = \mathbf{E} \cdot \boldsymbol{x} \text{ on } \partial\Omega, \tag{18}$$

with

$$\Sigma^{\mathrm{I}} = \overline{\sigma}^{\mathrm{I}} = \mathbb{C}^* : \mathbf{E} \tag{19}$$

where the macroscopic stress tensor, $\Sigma = \overline{\sigma}$,[43] and $\mathbb{C}^* = \overline{\mathbb{C} : \mathbb{A}} : \mathbf{E}$ are the upscaled stiffness tensors for the dual-material. Subproblem II defines a constrained material, $\mathbf{E} = 0$, subject to loading via the prestress field, $\boldsymbol{\sigma}^p$, as follows:

$$\nabla \cdot \boldsymbol{\sigma}^{\mathrm{II}} = 0 \text{ in } \Omega, \tag{20}$$

$$\boldsymbol{\sigma}^{\mathrm{II}} = \mathbb{C}(\boldsymbol{x}) : \boldsymbol{\epsilon}^{\mathrm{II}} + \boldsymbol{\sigma}^p(\boldsymbol{x}) \text{ in } \Omega, \tag{21}$$

$$\hat{\boldsymbol{u}}^{\mathrm{II}} = 0 \text{ on } \partial\Omega, \tag{22}$$

with

$$\Sigma^{\mathrm{II}} = \overline{\sigma}^{\mathrm{II}} = \overline{\mathbb{C}(\boldsymbol{x}) : \boldsymbol{\epsilon}^{\mathrm{I}}} + \overline{\sigma^{p}(\boldsymbol{x})}. \tag{23}$$

From Dormieux et al,[21] one can show

$$\Sigma^{\mathrm{II}} = \Sigma^{p}, \tag{24}$$

where $\Sigma^{p} = \overline{\sigma^{p} : \mathbb{A}}$. Equation (24) is a part of a classical result in micromechanics referred to as Levin's theorem.[45] That is, the macroscopic constitutive equation follows the form of the linear local constitutive relation, Equation (3),

$$\Sigma = \Sigma^{\mathrm{I}} + \Sigma^{\mathrm{II}} = \mathbb{C}^{*} : \mathbf{E} + \Sigma^{p}, \tag{25}$$

where we make use of the linearity of the problem to superpose subproblems I and II. Owing to the definition of $\mathbb{C}(\boldsymbol{x})$, and from Equations (14) and (15), the homogenised stiffness tensor of the composite dual-material is defined as

$$\mathbb{C}^{*} = v_m \overline{\mathbb{A}}_m : \mathbb{C}_m + (\mathbb{I} - v_m \overline{\mathbb{A}}_m) : \mathbb{C}_f. \tag{26}$$

Similarly, the homogenised prestress tensor is given as

$$\Sigma^{p} = -v_m \overline{\mathbb{A}}_m : \boldsymbol{b}_m P_m - (\mathbb{I} - v_m \overline{\mathbb{A}}_m) : \boldsymbol{b}_f P_f. \tag{27}$$

Intuitively, Equation (27) can be interpreted as a weighted sum of the continuum pressures. In the work of Borja and Koliji,[46] they derive a pore fraction weighting formulation that is thermodynamically consistent. Such an approach was also proposed in Coussy.[40] Given the thermodynamic consistency, it would be interesting to see how one could recover a pore fraction weighted formulation within the general framework of microporomechanics.

To proceed, using Equation (27), and with the result from Equation (26), we can identify the first of the macroscopic constitutive parameters, that is, the effective Biot coefficients,

$$\boldsymbol{B}_m = \boldsymbol{b}_m : \left[ \left( \mathbb{C}^{*} - \mathbb{C}_f \right) : \left( \mathbb{C}_m - \mathbb{C}_f \right)^{-1} \right], \tag{28}$$

$$\boldsymbol{B}_f = \boldsymbol{b}_f : \left( \mathbb{I} - \boldsymbol{b}_f \right) : \left[ \left( \mathbb{C}^{*} - \mathbb{C}_f \right) : \left( \mathbb{C}_m - \mathbb{C}_f \right)^{-1} \right]. \tag{29}$$

From the energy approach to poromechanics,[40] the DC model requires state equations for the evolutions of macroscopic Lagragian porosity.[22] Accordingly, for subproblem I,

$$\begin{aligned} \mathrm{d}\phi_{\alpha}^{\mathrm{I}} = v_{\alpha} \overline{\mathrm{d}\varphi_{\alpha}} \quad &= v_{\alpha} \overline{\mathbb{A}}_{\alpha} : \boldsymbol{b}_{\alpha} : \mathbf{E} \\ &= \boldsymbol{B}_{\alpha} : \mathbf{E}, \end{aligned} \tag{30}$$

where we have made use of Equation (4) in defining Equation (30).

Given subproblem II, we have

$$\mathrm{d}\phi_{m}^{\mathrm{II}} = v_m \boldsymbol{b}_m : \overline{\boldsymbol{\epsilon}}_{m}^{\mathrm{II}} + \frac{v_m}{n_m} P_m, \tag{31}$$

$$\mathrm{d}\phi_{f}^{\mathrm{II}} = -v_m \boldsymbol{b}_f : \overline{\boldsymbol{\epsilon}}_{m}^{\mathrm{II}} + \frac{v_f}{n_f} P_f, \tag{32}$$

where we have used Equation (11) together with the fact $\overline{\boldsymbol{\epsilon}}^{\mathrm{II}} = 0$ to eliminate $v_f \overline{\boldsymbol{\epsilon}}_f$. To advance, we must substitute for $v_m \overline{\boldsymbol{\epsilon}}_m^{\mathrm{II}}$. Following Dormieux et al,[21] $v_m \overline{\boldsymbol{\epsilon}}_m^{\mathrm{II}}$ can be expressed as

$$v_m \overline{\boldsymbol{\epsilon}}_m^{\mathrm{II}} = \left(\mathbb{C}_m - \mathbb{C}_f\right)^{-1} : \left[\left(v_m \boldsymbol{b}_m - \boldsymbol{B}_m\right) P_m + \left(v_f \boldsymbol{b}_f - \boldsymbol{B}_f\right) P_f\right]. \tag{33}$$

With Equation (33) in Equations (31) and (32), we recover

$$\mathrm{d}\phi_m^{\mathrm{II}} = \frac{1}{N_m} P_m + \frac{1}{Q_m} P_f, \tag{34}$$

$$\mathrm{d}\phi_f^{\mathrm{II}} = \frac{1}{Q_f} P_m + \frac{1}{N_f} P_f, \tag{35}$$

where the effective constitutive parameters $N_\alpha^{-1}$ and $Q_\alpha^{-1}$ are defined as

$$\frac{1}{N_m} = \boldsymbol{b}_m : \left[\left(v_m \boldsymbol{b}_m - \boldsymbol{B}_m\right) : \left(\mathbb{C}_m - \mathbb{C}_f\right)^{-1}\right] + \frac{v_m}{n_m}, \tag{36}$$

$$\frac{1}{Q_m} = \boldsymbol{b}_m : \left[\left(v_f \boldsymbol{b}_f - \boldsymbol{B}_f\right) : \left(\mathbb{C}_m - \mathbb{C}_f\right)^{-1}\right], \tag{37}$$

$$\frac{1}{N_f} = \boldsymbol{b}_f : \left[\left(\boldsymbol{B}_f - v_f \boldsymbol{b}_f\right) : \left(\mathbb{C}_m - \mathbb{C}_f\right)^{-1}\right] + \frac{v_f}{n_f}, \tag{38}$$

$$\frac{1}{Q_f} = \boldsymbol{b}_f : \left[\left(\boldsymbol{B}_m - v_m \boldsymbol{b}_m\right) : \left(\mathbb{C}_m - \mathbb{C}_f\right)^{-1}\right]. \tag{39}$$

Provided that the storage continuum is isotropic, $Q_m^{-1} = Q_f^{-1}$ since $\boldsymbol{b}_m = b_m \mathbf{1}$, where $\mathbf{1}$ is the second-order identity tensor.[21]

Finally, through superposition of subproblems I and II for the macroscopic variables $\boldsymbol{\Sigma}$ and $\mathrm{d}\phi_\alpha$, we recover the anisotropic, dual-stiffness constitutive model for the dual-scale, poroelastic material as

$$\Sigma = \mathbb{C}^* : \mathbf{E} - \boldsymbol{B}_m P_m - \boldsymbol{B}_f P_f, \tag{40}$$

$$\mathrm{d}\phi_m = \boldsymbol{B}_m : \mathbf{E} + \frac{1}{N_m} P_m + \frac{1}{Q_m} P_f, \tag{41}$$

$$\mathrm{d}\phi_f = \boldsymbol{B}_f : \mathbf{E} + \frac{1}{Q_f} P_m + \frac{1}{N_f} P_f, \tag{42}$$

where expressions for the effective constitutive parameters $\mathbb{C}^*$, $\boldsymbol{B}_m$, $\boldsymbol{B}_f$, $N_m^{-1}$, $Q_m^{-1}$, $N_f^{-1}$ and $Q_f^{-1}$ are given by Equations (26), (28), (29) and (36) to (39), respectively.

### 2.2.3 | Model equivalencies

Under certain conditions, the parameter models just referenced reduce to other mechanical property-based parameter models proposed in literature. For example, in the case of soils, the high-permeability (transport) continuum is all void space.[47] As a result $\mathbb{C}_f = 0$, and we recover the original anisotropic parameter models proposed by.[21] For an isotropic material, the constitutive system can be written in terms of scalar invariants of the tensorial quantities.

Accordingly, with a change from the mixed-compliance constitutive formulation to a pure-stiffness formulation, we recover the dual-stiffness models introduced by previous studies.[17,22] Using parameter models by Berryman,[17] we show some possible situations in which the inclusion of intrinsic fracture stiffness properties may be important. Further, in Kim et al,[48] the authors show use of Berryman[17]-type coefficient models lead to well-posed mathematical problems, an important consideration for numerical modelling. Finally, combining the void space transport and isotropic dual-material assumptions allows us to recover parameter models originally proposed by Berryman and Wang[6] and Khalili and Valliappan.[8]

Under long-term drainage, $P_m = P_f$, DC models should reduce to single-continuum equivalents.[6] As a result, we recover the following compatibility relations:

$$\boldsymbol{B} = \boldsymbol{1} - \mathbb{C}^* : \mathbb{C}_s^{-1} : \boldsymbol{1} = \boldsymbol{B}_m + \boldsymbol{B}_f, \tag{43}$$

$$\frac{1}{N} = (\boldsymbol{B} - \phi \boldsymbol{1}) : \mathbb{C}_s^{-1} : \boldsymbol{1} = \frac{1}{N_m} + \frac{1}{N_f} + \frac{1}{Q_m} + \frac{1}{Q_f}, \tag{44}$$

where $\mathbb{C}_s$ is the solid-grain stiffness tensor and $\phi = \phi_m + \phi_f$. Equations (43) and (44) hold, provided that $\mathbb{C}_s$ is the same for both the matrix and fracture continua. Accordingly, applying the long-term drainage condition and contracting Equations (40) to (42), we recover the single-porosity constitutive model originally proposed in Biot,[39] albeit for anisotropic materials. Alternatively, we could recover the single-porosity model by setting $v_f = 0$, and thus $\mathbb{C}_f = 0$ with $\mathbb{C}^* = \mathbb{C}_m$.

## 3 | NUMERICAL FRAMEWORK

Here, we introduce the computational framework used for modelling the coupled DC problem. We start by introducing the strong form of the DC poroelastic problem and then progressing to its fully discrete counterpart.

### 3.1 | Strong form

In addition to Equations (40) to (42), we require constitutive relations for intracontinuum and intercontinuum mass flux terms, $\boldsymbol{w}_\alpha$ and $\gamma_\alpha$, respectively. Intracontinuum mass flux is given according to Darcy's law,

$$\boldsymbol{w}_\alpha = \rho_l \boldsymbol{q}_\alpha = -\rho_l \frac{\boldsymbol{k}_\alpha^*}{\mu_l} \cdot (\nabla P_\alpha - \rho_l \boldsymbol{g}), \tag{45}$$

where $\boldsymbol{q}_\alpha$ is the volumetric flux vector associated with continuum $\alpha$, $\rho_l$ and $\mu_l$ are the intrinsic fluid density and fluid viscosity respectively, $\boldsymbol{g}$ is the gravity vector and $\boldsymbol{k}_\alpha^*$ is the macroscopic continuum permeability tensor. The intercontinuum mass flux, $\gamma_\alpha$, is given according to a first-order transfer term originally proposed by Warren and Root,[49]

$$\gamma_\alpha = \rho_l \frac{\varkappa k'}{\mu_l} (P_\beta - P_\alpha), \tag{46}$$

where $k'$ denotes the interface permeability, taken here as the intrinsic matrix permeability,[1,7] and $\varkappa$ is a parameter referred to as the shape factor.[49] In this work, we use an analytically derived $\varkappa$ for an isotropic matrix given according to Lim and Aziz,[50]

$$\varkappa = \frac{N\pi^2}{s^2}, \tag{47}$$

where $N$ is a dimension parameter related to the number of fracture sets and $s$ is the characteristic spacing length of the fracture continuum (Figure 1).

Finally, we give the compatibility between the macroscopic linearised strain tensor and macroscopic displacement, $\boldsymbol{U}$, as

$$\mathbf{E} = \underline{\nabla}\boldsymbol{U} = \frac{1}{2}(\nabla \boldsymbol{U} + \nabla^{\top}\boldsymbol{U}), \tag{48}$$

where we introduce notation $\underline{\nabla}$ to denote the symmetric gradient operator on $\boldsymbol{U}$.

The conservation equations considered for the DC poroelastic problem are the momentum equation

$$\nabla \cdot \Sigma + \rho \boldsymbol{g} = \tilde{\gamma} \tag{49}$$

and the continuity equations for each continuum

$$\frac{\partial m_{l,m}}{\partial t} + \nabla \cdot \boldsymbol{w}_m = \gamma_m, \tag{50}$$

$$\frac{\partial m_{l,f}}{\partial t} + \nabla \cdot \boldsymbol{w}_f = \gamma_f. \tag{51}$$

Notations $\rho$ and $\tilde{\gamma}$ in Equation (49) are the bulk density of the dual-material, and a momentum source arising from the intercontinuum mass transfer, respectively. For the remainder, we assume $\tilde{\gamma} \approx 0$, with respect to the other force density terms in Equation (49). Notation $m_{l,\alpha}$ in Equations (50) and (51) is the fluid mass content associated with continuum $\alpha$. The fluid mass content is given by $m_{l,\alpha} = \rho_l \phi_\alpha$.

We consider the conservation equations over a domain, $\Omega^{\mathcal{D}} \subset \mathbb{R}^2$, bounded by $\partial\Omega^{\mathcal{D}}$. The domain boundary is separated into disjoint boundary segments corresponding to Dirichlet and Neumann boundary conditions for the mechanical and flow problems. For the mechanical problem, this implies displacement ($\Gamma^{\mathrm{U}}$) and traction ($\Gamma^{\mathrm{T}}$) boundary conditions. To ensure well-posedness, $\Gamma^{\mathrm{U}} \cup \Gamma^{\mathrm{T}} = \partial\Omega^{\mathcal{D}}$ and $\Gamma^{\mathrm{U}} \cap \Gamma^{\mathrm{T}} = \varnothing$. For the flow problem, the boundary conditions for a given continuum are pressure ($\Gamma^{\mathrm{P}}_{\alpha}$) and flux ($\Gamma^{\mathrm{Q}}_{\alpha}$). Again, for a well-posed problem, we have $\Gamma^{\mathrm{P}}_{\alpha} \cup \Gamma^{\mathrm{Q}}_{\alpha} = \partial\Omega^{\mathcal{D}}$ and $\Gamma^{\mathrm{P}}_{\alpha} \cap \Gamma^{\mathrm{Q}}_{\alpha} = \varnothing$.

The strong form is finally defined as follows: Find $\boldsymbol{U}$, $P_m$ and $P_f$ that satisfy Equations (49) to (51) subject to the following boundary conditions:

$$\boldsymbol{U} = \hat{\boldsymbol{U}} \text{ on } \Gamma^{\mathrm{U}}, \tag{52}$$

$$\Sigma \cdot \boldsymbol{n} = \hat{\boldsymbol{T}} \text{ on } \Gamma^{\mathrm{T}}, \tag{53}$$

$$P_m = \hat{P}_m \text{ on } \Gamma^{\mathrm{P}}_m, \tag{54}$$

$$\boldsymbol{q}_m \cdot \boldsymbol{n} = \hat{q}_m \text{ on } \Gamma^{\mathrm{Q}}_m, \tag{55}$$

$$P_f = \hat{P}_f \text{ on } \Gamma^{\mathrm{P}}_f, \tag{56}$$

$$\boldsymbol{q}_f \cdot \boldsymbol{n} = \hat{q}_f \text{ on } \Gamma^{\mathrm{Q}}_f, \tag{57}$$

with initial conditions

$$\boldsymbol{U} = \boldsymbol{U}^0,\ P_m = P^0_m,\ P_f = P^0_f, \tag{58}$$

for all $(\boldsymbol{X}, t) \in (\Omega^{\mathcal{D}} \times t = 0)$. Notation $\boldsymbol{X}$ is the macroscopic position vector.

The single porosity linear poroelastic model can be recovered from Equations (49) to (58) under the assumption $P = P_m = P_f$ and combining Equations (50) and (51). With the contraction to a single-continuum system, DC constitutive parameters reduce to single-porosity equivalents, Equations (43) and (44).

## 3.2 | Weak form

The weak formulation of the strong form introduced previously requires the definition of the appropriate function spaces. Accordingly, solution spaces for continuum pressure and the displacements are $\mathcal{S}_{P_\alpha} = L^2(\Omega^{\mathcal{D}})$ and $\mathcal{S}_U = \{\boldsymbol{U} \in H^1(\Omega^{\mathcal{D}})^d : \boldsymbol{U} = \hat{\boldsymbol{U}} \text{ on } \Gamma^{\mathrm{U}}\}$, respectively, where $L^2$ and $H^1$ are the typical square integrable and first-order Sobolev function spaces. Weighting function spaces are then defined as $\mathcal{W}_{P_\alpha} = L^2(\Omega^{\mathcal{D}})$ and $\mathcal{W}_U = \{\eta \in H^1(\Omega^{\mathcal{D}})^d : \eta = \boldsymbol{0} \text{ on } \Gamma^{\mathrm{U}}\}$.

To progress, we substitute the constitutive equations, Equations (40) to (42), (45) and (46), and macroscopic strain compatibility relation, Equation (48), into Equations (49) to (51). We adopt the material and fluid assumptions introduced in Section 2 whilst also neglecting gravitational effects. Assuming isotropic matrix material results in $Q_m^{-1} = Q_f^{-1} = Q^{-1}$ and $\boldsymbol{B}_m = B_m \mathbf{1}$. Further, we restrict our anisotropic experiments to orthotropic materials. Finally, comparing trial functions against weight functions, the weak form is defined as follows: Find $(\boldsymbol{U}, P_m, P_f) \in (\mathcal{S}_U \times \mathcal{S}_{P_m} \times \mathcal{S}_{P_f})$ such that for all $(\eta, \omega_m, \omega_f) \in (\mathcal{W}_U \times \mathcal{W}_{P_m} \times \mathcal{W}_{P_f})$,

$$\begin{aligned} g(\eta, \boldsymbol{U}) - \int_{\Omega^{\mathcal{D}}} (\nabla \eta) \cdot \boldsymbol{B}_m P_m \, \mathrm{d}V - \int_{\Omega^{\mathcal{D}}} (\nabla \eta) \cdot \boldsymbol{B}_f P_f \, \mathrm{d}V \\ = \int_{\Gamma^{\mathrm{T}}} \eta \cdot \hat{\boldsymbol{T}} \, \mathrm{d}S, \end{aligned} \tag{59}$$

$$\begin{aligned} \int_{\Omega^{\mathcal{D}}} \frac{\partial}{\partial t} \omega_m \left( \boldsymbol{B}_m : \underline{\nabla} \boldsymbol{U} + \frac{1}{M_m} P_m + \frac{1}{Q} P_f \right) \mathrm{d}V \\ - \int_{\Omega^{\mathcal{D}}} \omega_m \nabla \cdot \left( \frac{\boldsymbol{k}_m^*}{\mu_l} \cdot \nabla P_m \right) \mathrm{d}V = \int_{\Omega^{\mathcal{D}}} \omega_m \frac{\varkappa k'}{\mu_l} (P_f - P_m) \mathrm{d}V, \end{aligned} \tag{60}$$

$$\begin{aligned} \int_{\Omega^{\mathcal{D}}} \frac{\partial}{\partial t} \omega_f \left( \boldsymbol{B}_f : \underline{\nabla} \boldsymbol{U} + \frac{1}{Q} P_m + \frac{1}{M_f} P_f \right) \mathrm{d}V \\ - \int_{\Omega^{\mathcal{D}}} \omega_f \nabla \cdot \left( \frac{\boldsymbol{k}_f^*}{\mu_l} \cdot \nabla P_f \right) \mathrm{d}V = \int_{\Omega^{\mathcal{D}}} \omega_f \frac{\varkappa k'}{\mu_l} (P_m - P_f) \mathrm{d}V. \end{aligned} \tag{61}$$

The bilinear form $g(\cdot\,, \cdot)$ in Equation (59) is given by

$$g(\eta, \boldsymbol{U}) = \int_{\Omega^{\mathcal{D}}} \underline{\nabla} \eta : \Sigma'(\boldsymbol{U}) \mathrm{d}V, \tag{62}$$

where $\Sigma'(\boldsymbol{U}) = \mathbb{C}^* : \underline{\nabla} \boldsymbol{U}$ is the effective stress tensor. The term $M_\alpha^{-1}$ in Equations (60) and (61) is given as

$$\frac{1}{M_\alpha} = \frac{1}{N_\alpha} + \frac{\phi_\alpha^0}{K_l}, \tag{63}$$

where $K_l$ is the fluid bulk modulus.

## 3.3 | Discrete block matrix form

The discrete counterpart to Equations (59) to (61) is formulated using the finite-volume method (FVM) for flow, the virtual-element method (VEM) for mechanics[51,52] and the backward Euler method for time. This hybrid numerical approach to poroelasticity was originally developed using the Matlab Reservoir Simulation Toolbox (MRST)[53,54] by previous studies[55,56] for single-continuum materials and later expanded in Ashworth and Doster[57] to DC materials. We use this hybrid framework in the current work due to its availability. However, recent works have shown the current

modelling framework to be suitable for subsurface applications where complex geometrical structures can lead to irregular grids not easily handled by standard finite-element methods.[56,58]

We partition our domain into disjoint elements (or cells). Accordingly, for the DC problem, $\Omega^{\mathcal{D}} = \cup_{j=1}^{n_{elem}} \Omega_j^{\mathcal{D}}$, where $n_{elem}$ is the number of elements. Notation $\Omega_j^{\mathcal{D}}$ denotes the DC element for which there are *two* pressure degrees of freedom, corresponding to each continuum.

We define the following discrete solution spaces for the DC problem as $\mathcal{S}_{P_\alpha}^h \subset \mathcal{S}_{P_\alpha}$ and $\mathcal{S}_U^h \subset \mathcal{S}_U$. Discrete weighting spaces are given as $\mathcal{W}_{P_\alpha}^h \subset \mathcal{W}_{P_\alpha}$ and $\mathcal{W}_U^h \subset \mathcal{W}_U$. Discrete continuum pressure fields, $P_\alpha^h \in \mathcal{S}_{P_\alpha}^h$, and discrete displacement fields, $\boldsymbol{U}^h \in \mathcal{S}_U^h$, are given according to the following interpolation relations, respectively:

$$P_\alpha^h = \sum_{j=1}^{n_{elem}} \mathbb{P}^j \tilde{P}_\alpha^j, \tag{64}$$

$$\boldsymbol{U}^h = \sum_{b=1}^{n_{node}} \mathbb{N}^b \tilde{\boldsymbol{U}}^b, \tag{65}$$

where $n_{node}$ denotes the total number of vertices and $\tilde{P}_\alpha^j$ and $\tilde{\boldsymbol{U}}^b$ are pressure and displacement degrees of freedom respectively, with the corresponding basis functions denoted by $\mathbb{P}^j$ and $\mathbb{N}^b$.

In FVM, we consider $\tilde{P}_\alpha^j$ to be cell-centred quantities. Notation $\mathbb{P}^j$ is then an indicator function for continuum $\alpha$ given as

$$\mathbb{P}^j(\boldsymbol{X}) = \begin{cases} 1 & \text{if } \boldsymbol{X} \text{ in } \Omega_j^{\mathcal{D}} \\ 0 & \text{otherwise} \end{cases}. \tag{66}$$

Further, we replace discrete pressure weight functions, $\omega_\alpha^h \in \mathcal{W}_{P_\alpha}^h$, by the indicator function whilst also using Equation (64) such that Equations (60) and (61) can be interpreted as element-wise conservation statements. Using Gauss's theorem, element-wise divergence of flux volume integrals in Equations (60) and (61) are turned into face-wise surface integrals. In this work, we use the two-point flux approximation to calculate these face-wise flux integrals (see Lie[53] for further details).

The nodal basis function matrix, $\mathbb{N}^b$, takes the identity matrix $\mathbf{1}$ when located at node $b$ and $\mathbf{0}$ at all other nodes. VEM is a Galerkin-based method, thus the discrete displacement weight, $\eta^h \in \mathcal{W}_U^h$, is an interpolation of the type shown in Equation (65). However, in VEM, contrary to standard finite-element methods, the bilinear form with discrete fields can never be directly calculated, as basis functions are never explicitly defined. Due to basis function independence, VEM can be interpreted as a generalisation of the finite-element method to arbitrary polygonal and polyhedral meshes. Such a property is desirable for subsurface modelling, where degenerate cells and hanging nodes are encountered.[56] Instead, the idea in VEM is to approximate the bilinear form, such that

$$g(\eta^h, \boldsymbol{U}^h) \approx g^h(\eta^h, \boldsymbol{U}^h), \tag{67}$$

where $g^h(\eta^h, \boldsymbol{U}^h) = \sum_{j=1}^{n_{elem}} g_j^h(\eta^h, \boldsymbol{U}^h)$ and where details of the element-wise first-order bilinear VEM approximation, $g_j^h(\eta^h, \boldsymbol{U}^h)$, can be found in Gain et al[52] and Andersen et al.[56] Finally, as part of the VEM assembly, the constitutive relation, Equation (62), need only be computed once, similar to a one-point quadrature finite-element scheme.[59]

Replacing solutions and weighting functions with their discrete counterparts, and using the time discretisation, the discrete residual equations from Equations (59) and (60) are

$$\begin{aligned} \boldsymbol{R}_U^a &= g^h(\mathbb{N}^a, \boldsymbol{U}^{h,n+1}) - \int_{\Omega^{\mathcal{D}}} (\nabla \mathbb{N}^a) \cdot \boldsymbol{B}_m P_m^{h,n+1} \mathrm{d}V \\ &\quad - \int_{\Omega^{\mathcal{D}}} (\nabla \mathbb{N}^a) \cdot \boldsymbol{B}_f P_f^{h,n+1} \mathrm{d}V - \int_{\Gamma^{\mathrm{T}}} \mathbb{N}^a \cdot \hat{\boldsymbol{T}} \mathrm{d}S \\ &= \boldsymbol{0}, \forall a = 1, \ldots, n_{node}, \end{aligned} \tag{68}$$

$$
\begin{aligned}
R^i_{P_m} &= \int_{\Omega_i^{\mathcal{D}}} \boldsymbol{B}_m \cdot \Delta\left(\underline{\nabla}\boldsymbol{U}^{h,n+1}\right) + \frac{1}{M_m}\Delta P_m^{h,n+1} + \frac{1}{Q}\Delta P_f^{h,n+1}\,\mathrm{d}V \\
&\quad - \Delta t \int_{\partial\Omega_i^{\mathcal{D}}} \left(\frac{\boldsymbol{k}_m^*}{\mu_l}\cdot\nabla P_m^{h,n+1}\right)\cdot\boldsymbol{n}\,\mathrm{d}S \\
&\quad - \Delta t \int_{\Omega_i^{\mathcal{D}}} \frac{\varkappa k'}{\mu_l}(P_f^{h,n+1} - P_m^{h,n+1})\,\mathrm{d}V \\
&= 0,\ \forall i = 1,\ldots,n_{elem},
\end{aligned}
\tag{69}
$$

$$
\begin{aligned}
R^i_{P_f} &= \int_{\Omega_i^{\mathcal{D}}} \left(\boldsymbol{B}_f \cdot \Delta\left(\underline{\nabla}\boldsymbol{U}^{h,n+1}\right) + \frac{1}{Q}\Delta P_m^{h,n+1} + \frac{1}{M_f}\Delta P_f^{h,n+1}\right)\mathrm{d}V \\
&\quad - \Delta t \int_{\partial\Omega_i^{\mathcal{D}}} \left(\frac{\boldsymbol{k}_f^*}{\mu_l}\cdot\nabla P_f^{h,n+1}\right)\cdot\boldsymbol{n}\,\mathrm{d}S \\
&\quad - \Delta t \int_{\Omega_i^{\mathcal{D}}} \frac{\varkappa k'}{\mu_l}(P_m^{h,n+1} - P_f^{h,n+1})\,\mathrm{d}V \\
&= 0,\ \forall i = 1,\ldots,n_{elem},
\end{aligned}
\tag{70}
$$

where we make use of Voigt notation for tensor representation. Notation $\Delta\boldsymbol{z}^{n+1} = \boldsymbol{z}^{n+1} - \boldsymbol{z}^n$, where $n$ denotes the vcurrent time level. Details of the VEM calculations for the boundary and gradient terms involving $\mathbb{N}^a$ in Equation (68) can be found in Andersen et al.[56]

Even though we assume linearity in the current work, poroelastic problems are generally nonlinear due to material and geometric nonlinearities. To provide a general numerical framework, we therefore present the discrete equations describing the DC problem following application of Newton's method. In MRST, this is handled naturally using an automatic differentation framework to generate the Jacobian. We give the discrete system of equations in block matrix form as

$$
\begin{bmatrix} \boldsymbol{K} & -\boldsymbol{D}_m^\top & -\boldsymbol{D}_f^\top \\ \boldsymbol{D}_m & \boldsymbol{F}_m & \boldsymbol{E}_m \\ \boldsymbol{D}_f & \boldsymbol{E}_f & \boldsymbol{F}_f \end{bmatrix}^{(l)} \begin{bmatrix} \delta\tilde{\boldsymbol{U}} \\ \delta\tilde{\boldsymbol{P}}_m \\ \delta\tilde{\boldsymbol{P}}_f \end{bmatrix}^{n+1,(l)} = - \begin{bmatrix} \boldsymbol{R}_U \\ \boldsymbol{R}_{P_m} \\ \boldsymbol{R}_{P_f} \end{bmatrix}^{n+1,(l)},
\tag{71}
$$

where $\boldsymbol{R}_U = [\boldsymbol{R}_U^1,\ldots,\boldsymbol{R}_U^{n_{node}}]^\top$ and $\boldsymbol{R}_{P_\alpha} = [R_{P_\alpha}^1,\ldots,R_{P_\alpha}^{n_{elem}}]^\top$. Notations $\delta$ and $l$ denote the change in solution and current iteration levels, respectively. Further, $\tilde{\boldsymbol{U}} = [\tilde{\boldsymbol{U}}^1,\ldots,\tilde{\boldsymbol{U}}^{n_{node}}]^\top$ and $\tilde{\boldsymbol{P}}_\alpha = [\tilde{P}_\alpha^1,\ldots,\tilde{P}_\alpha^{n_{elem}}]^\top$. The individual matrices comprising the Jacobian in Equation (71) are given as

$$
\boldsymbol{K}_{ab} = \frac{\partial \boldsymbol{R}_U^a}{\partial \tilde{\boldsymbol{U}}^b} = g^h(\mathbb{N}^a,\mathbb{N}^b),
\tag{72}
$$

$$
\boldsymbol{D}_{ib,\alpha} = \frac{\partial R^i_{P_\alpha}}{\partial \tilde{\boldsymbol{U}}^b} = \int_{\Omega^{\mathcal{D}}} \mathbb{I}^i(\boldsymbol{X}_i)\boldsymbol{B}_\alpha\cdot\nabla\mathbb{N}^b\,\mathrm{d}V,
\tag{73}
$$

$$
\begin{aligned}
\boldsymbol{E}_{ij,\alpha} = \frac{\partial R^i_{P_\alpha}}{\partial \tilde{P}^j_\beta} &= \int_{\Omega^{\mathcal{D}}} \mathbb{I}^i(\boldsymbol{X}_i)\frac{1}{Q}\mathbb{I}^j(\boldsymbol{X}_i)\,\mathrm{d}V \\
&\quad - \Delta t \int_{\Omega^{\mathcal{D}}} \mathbb{I}^i(\boldsymbol{X}_i)\frac{\varkappa k'}{\mu_l}\mathbb{I}^j(\boldsymbol{X}_i)\,\mathrm{d}V,
\end{aligned}
\tag{74}
$$

$$
\begin{aligned}
\boldsymbol{F}_{ij,\alpha} = \frac{\partial R^i_{P_\alpha}}{\partial \tilde{P}^j_\alpha} &= \int_{\Omega^{\mathcal{D}}} \mathbb{I}^i(\boldsymbol{X}_i)\frac{1}{M_\alpha}\mathbb{I}^j(\boldsymbol{X}_i)\,\mathrm{d}V \\
&\quad + \Delta t \int_{\Omega^{\mathcal{D}}} \mathbb{I}^i(\boldsymbol{X}_i)\frac{\varkappa k'}{\mu_l}\mathbb{I}^j(\boldsymbol{X}_i)\,\mathrm{d}V + \Delta t\boldsymbol{G}_{ij,\alpha},
\end{aligned}
\tag{75}
$$

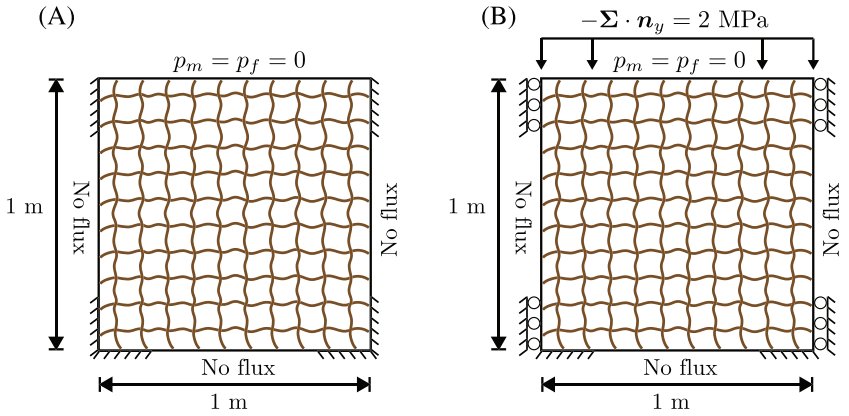


**FIGURE 2** Conceptual illustrations of the geometries and boundary conditions for (A) the undeformable isotropic problem and (B) the deformable isotropic problem. In (B), the base is fixed whilst the left, right and top boundaries can move vertically [Colour figure can be viewed at wileyonlinelibrary.com]

where $\boldsymbol{X}_i$ denotes the centroid of element $\Omega_i^{\mathcal{D}}$ and $\boldsymbol{G}_{ij,\alpha}$ is the transmissibility matrix for continuum $\alpha$ arising from the two-point flux approximation.[53]

Finally, Equation (71) is solved using a fully coupled approach,[60] although extensions to sequential solution strategies for DC materials have been shown in Kim et al[48] and Ashworth and Doster.[57]

## 4 | NUMERICAL TESTS

With the framework in-hand, we present and conduct the numerical tests used to investigate whether the macroscopic DC poroelastic model can capture global flow and deformation behaviours of a FS explicit model. In doing, we review several considerations for the interpretation of the results at the scale of the DC model.

### 4.1 | Test cases

We introduce four numerical experiments to test the validity of the DC poroelastic concept. In each case, we consider an idealised representation of a naturally fractured rock sample. Our idealisation comes in that we assume the fracture fabric to be periodic. To start, we consider an undeformable isotropic material to understand the physics of the flow problem. We progress by introducing mechanics to the isotropic system and then adding complexity by considering anisotropic material cases.

In every case, we consider the dimension of the domain to be 1 m × 1 m. Each experiment then represents a thin 2D slice taken from a 3D sample such that, in the case of the mechanical problem, the plane-stress assumption applies.

#### 4.1.1 | Undeformable isotropic

For this test, we study an (isotropic) undeformable matrix permeated by an isotropic undeformable fracture network. The test is setup as a uniaxial drainage problem, such that the top boundary is open to flow, $\hat{P}_m = \hat{P}_f = 0$, whilst the left, right and bottom boundaries are zero flux boundaries (Figure 2A). Initial pressures for the continua are set at $P_m^0 = P_f^0 = 2\text{MPa}$. Volume fractions for matrix and fracture material are $v_m = 0.998$ and $v_f = 0.002$, respectively, given a fracture spacing, $s$, of 0.1 m. Local porosities for the two continua are then prescribed as $\varphi_m = 0.1$ and $\varphi_f = 0.9$, where the volume fractions link the global and local Lagrangian porosities so that $\phi_\alpha = v_\alpha \varphi_\alpha$. Intrinsic matrix permeability, $k_m$, is taken as 0.01 md, whilst individual fracture permeability, $k_f$, is calculated using the parallel plate model with a fracture aperture of $a_f \approx 1.05 \times 10^{-4}$ m.[61] The resulting permeability is 950 d for each fracture.* Fluid properties are $\rho_l = 1{,}000\text{kgm}^{-3}$, $\mu_l = 1$ cp and $K_l = 2.5$ GPa. Upscaling individual fracture permeability to a continuum permeability for use in the DC model is done using the cubic law.[61] The resulting isotropic fracture continuum

*1 darcy (d) = $9.87 \times 10^{-13}$ m$^2$.

permeabitity is $k_f^* \approx 1{,}000\,\text{md}$. Finally, due to the dissociation by the fracture network, the macroscopic matrix permeability is zero.

### 4.1.2 | Deformable isotropic

We now consider a deformable counterpart to the experiment described in Section 4.1.1(Figure 2B). Accordingly, Young's moduli for the matrix and fracture materials are $E_m = 36$ GPa and $E_f = 36$ MPa, respectively. The latter is chosen for illustrative purposes as $E_f = E_m/1{,}000$. Both continua are assigned a Poisson's ratio of $\nu = 0.2$. For an isotropic medium under the plane-stress assumption, the stiffness tensor written with Voigt notation is given as

$$\mathbb{C} = \begin{bmatrix} \frac{E}{1-\nu^2} & \frac{\nu E}{1-\nu^2} & 0 \\ & \frac{E}{1-\nu^2} & 0 \\ sym & & G \end{bmatrix}, \tag{76}$$

where parameter $G = E/(2(1+\nu))$ is the shear modulus. Entries for $\mathbb{C}_m$ and $\mathbb{C}_f$ can be calculated with Equation (76) and the defined intrinsic parameter values.

For $\mathbb{C}^*$, parameters must be calculated by homogenisation. Ashworth and Doster[22] suggest using the Hashin-Shtrikman lower bounds[62] as an initial homogenisation approach for the estimation of the mechanical properties of densely fractured rock. For the bulk and shear moduli, these lower bounds are quoted as[62]

$$K^{HS^-} = K_f + \frac{v_m}{\left[(K_m - K_f)^{-1} + 3v_f(3K_f + 4G_f)^{-1}\right]}, \tag{77}$$

$$G^{HS^-} = G_f + \frac{v_m}{\left[(G_m - G_f)^{-1} + 6v_f(K_f + 2G_f)(5G_f(3K_f + 4G_f))^{-1}\right]}, \tag{78}$$

where $K_\alpha$ and $G_\alpha$ are the 3D bulk and shear moduli for continuum $\alpha$, respectively.

We map between the 3D bulk modulus calculated in Equation (77) and the 2D homogenised bulk modulus under plane-stress, $K^*$, using the following relation (e.g., Torquato[63]):

$$K^* = \frac{9K^{HS^-}G^{HS^-}}{3K^{HS^-} + 4G^{HS^-}}. \tag{79}$$

The Poissons ratio for the composite DC under plane-stress is given by

$$\nu^* = \frac{K^* - G^{HS^-}}{K^* + G^{HS^-}}. \tag{80}$$

Finally, the homogenised Young's modulus, $E^*$, can be recovered as

$$4K^* = \boldsymbol{1} : \mathbb{C}^* : \boldsymbol{1} = \frac{2E^*}{(1-\nu^*)}. \tag{81}$$

With Equations (80) and (81), the homogenised parameters are $\nu^* = 0.2$ and $E^* = 18.0$ GPa.

We assume the matrix and fracture skeletons to be made up of the same solid material. We then assign a solid modulus, $K_s$, of 70 GPa for both continua.

For the coupled mechanics and flow problem, we consider a different method of initialisation to Section 4.1.1. Instead of assigning initial continuum pressures, we define the starting point for the experiment to be the undrained,

loaded configuration, $P_m^{0+}$, $P_f^{0+}$, $\boldsymbol{U}^{0+}$. This undrained state is induced following the application of an instantaneous load on an unpressurised and undeformed domain, $P_m^0 = P_f^0 = 0$ and $\boldsymbol{U}^0 = 0$. Loading is prescribed as a vertical traction of $-\boldsymbol{\Sigma}\cdot\boldsymbol{n}_y = -2$ MPa on the top boundary. The domain is horizontally constrained at the boundaries but remains free to move along the vertical axis apart from at the bottom boundary where the sample is fixed. The parameters for flow are as defined in Section 4.1.1

### 4.1.3 | Geometry-induced anisotropy: Explicit computation of $\mathbb{C}^*$

The third experiment is concerned with an anisotropic deformable material. Anisotropy has recently been studied in poroelastic DC materials in the context of flow properties.[13] However, here we consider the directional dependence of *both* mechanical and flow properties. Anisotropy is introduced geometrically by considering just a single vertical fracture set which is aligned with the second principal axis (Figure 3a). The 2D domain is then orthotropic. Whilst anisotropy exists at the macroscale, the intrinsic mechanical parameters remain isotropic for each continuum and are as described in Section 4.1.2. The plane-stress stiffness tensor for an orthotropic material is given by

$$\mathbb{C} = \begin{bmatrix} \dfrac{E_1}{1-\nu_{12}\nu_{21}} & \dfrac{\nu_{21}E_1}{1-\nu_{12}\nu_{21}} & 0 \\ & \dfrac{E_2}{1-\nu_{12}\nu_{21}} & 0 \\ sym & & G_{12} \end{bmatrix}. \tag{82}$$

Parameters of the homogenised stiffness tensor may be approximated explicitly for this geometry, using mixture theory. Accordingly, for Young's moduli,

$$E_1^* = \left(\frac{v_m}{E_m} + \frac{v_f}{E_f}\right)^{-1}, E_2^* = v_m E_m + v_f E_f, \tag{83}$$

where having removed a fracture set, the volume fraction of the fracture continuum is now $v_f = 0.001$ (resp. $v_f = 0.999$). For the homogenised Poisson's ratio, $\nu_{21}^*$, and shear modulus, $G_{12}^*$, mixture theory gives

$$\nu_{21}^* = v_m\nu_m + v_f\nu_f,\ G_{12}^* = \left(\frac{v_m}{G_m} + \frac{v_f}{G_f}\right)^{-1}. \tag{84}$$

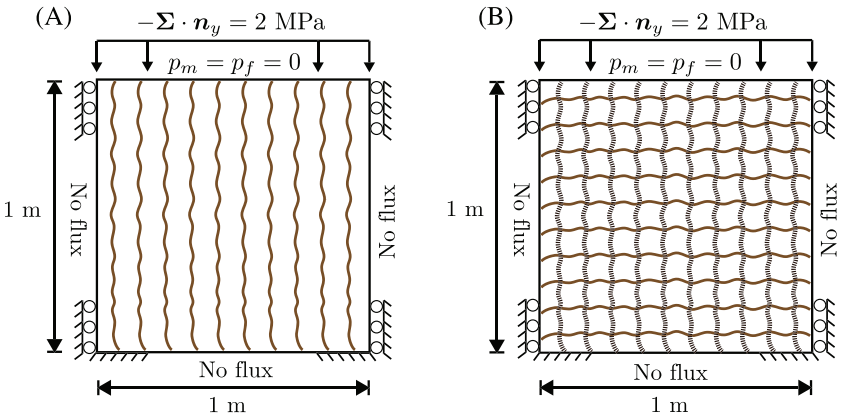


**FIGURE 3** Conceptual illustrations of the geometries and boundary conditions for (A) the anisotropic problem with one fracture set (and explicit computation of $\mathbb{C}^*$) and (B) the anisotropic problem with two fracture sets (and numerical computation of $\mathbb{C}^*$). In both cases, the bases are fixed whilst the left, right and top boundaries can move vertically [Colour figure can be viewed at wileyonlinelibrary.com]

The other Poisson's ratio, $\nu_{12}^*$, is readily determined by the symmetry in Equation (82), which requires $\nu_{12}E_2 = \nu_{21}E_1$. From Equations (83) and (84) and the aforementioned symmetry relation, the mechanical parameters are given as $E_1^* = 18.0\text{GPa}$, $E_2^* = 36.0\text{GPa}$, $\nu_{21}^* = 0.200$, $\nu_{12}^* = 0.100$ and $G_{12}^* = 7.50\text{GPa}$.

The anisotropic fracture continuum leads to an anistropic permeability tensor so that permeability in the $x$ and $y$ directions are $k_{f,x}^* = 0$ and $k_{f,y}^* \approx 1000\text{md}$, respectively. For the matrix, the macroscopic permeability is also anisotropic with $k_{m,x}^* = 0$ and $k_{m,y}^* \approx 0.01\text{md}$. The remaining flow parameters, boundary conditions and initialisation are as described in Sections 4.1.1 and 4.1.2.

### 4.1.4 | Material-induced anisotropy: Numerical computation of $\mathbb{C}^*$

The final experiment is on an anisotropic material with two fracture sets aligned with each of the principal axes (Figure 3B). Anisotropy is now introduced through the fracture material, with each fracture set having different intrinsic mechanical and flow properties. These property differences are in analogy to fractures containing different amounts of infill material. To represent this conceptually within the model, we assign different intrinsic porosities to the individual fracture sets. Further, we separate the intrinsic Young's moduli and permeabilities of each fracture set by two orders of magnitude. For the horizontal fracture set, we assign $\varphi_f^{\text{h}} = 0.9$, $E_f^{\text{h}} = 3.6\text{MPa}$ and an intrinsic fracture permeability of $k_f = 950$ d. For the vertical fracture set, we assign $\varphi_f^{\text{v}} = 0.4$, $E_f^{\text{v}} = 360\text{MPa}$ and an intrinsic permeability of 9.5 d. Upscaling the fracture permeability remains trivial, with $k_{f,x}^* \approx 1{,}000\text{md}$ and $k_{f,y}^* \approx 10\text{md}$. However, homogenistion for the parameters in the homogenised stiffness tensor now cannot be done by explicit approximation. Instead, we use a deformation-driven computational homogenisation approach: We generate unit strains for a sequence of linear displacement boundary conditions, and in doing, determine the entries of $\mathbb{C}^*$.[64] Linear displacements are chosen as they produce better estimates for effective stiffness tensors for materials with a stiff matrix and weaker inclusion material,[65] as is the case here.

With the computational homogenisation approach, the mechanical parameters in $\mathbb{C}^*$ are calculated as $E_1^* = 32.7\text{GPa}$, $E_2^* = 3.40\text{GPa}$, $\nu_{21}^* = 0.019$, $\nu_{12}^* = 0.173$ and $G_{12}^* = 1.28\text{GPa}$.

The overall volume fraction for the fracture continuum is the same as in experiment two. However, the intrinsic Lagrangian fracture porosity is now the arithmetic average of the two intrinsic fracture set porosities ($\varphi_f = 0.65$). Fluid and matrix properties remain the same as those for the other experiments. Boundary conditions and initialisation are the same as in experiments two and three.

## 4.2 | Modelling considerations

Here, we review several considerations to enable the interpretation of the test results to follow.

### 4.2.1 | On the REV

Our periodic assumption of the underlying microstructure eases the requirements on our definition for an REV. In this periodic case, all the necessary geometrical and physical process information are captured within an elementary cell that is the size of the heterogeneity ($s$).[21,66] The separation of scales is now defined as $s \ll L$. The elementary cell definition of our REV will be useful for interpreting the discretisation choice of the DC problem.

### 4.2.2 | Meshing

For the four tests, we discretise the FS problem with a $200 \times 200$ Cartesian mesh, which is locally refined around the fractures (Figure 4). For the DC problem, we discretise the domain using a $10 \times 10$ Cartesian mesh. In the latter case, each element then coincides with an elementary cell (in the geometrical sense) (Figure 4).

FS and DC fields are compared at an observation point at the base of our samples. At this point, we assume that our pressure solutions are sufficiently smooth, thus satisfying the physical process scale separation requirement. Further, the observation point coincides with the macroscopic material point, in this case the element centroid (Figure 4).

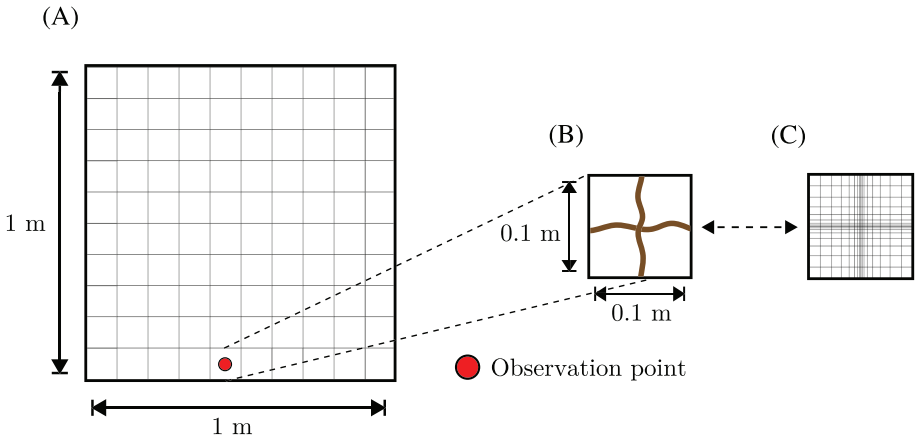


**FIGURE 4** Representations of the isotropic test problem: (A) the dual-continuum grid containing the observation point where the two modelling approaches are compared, (B) an elementary cell and (C) an equivalent fine-scale representation of the elementary cell [Colour figure can be viewed at wileyonlinelibrary.com]

### 4.2.3 | Quantities of interest

At each test observation point, we consider the element-wise total and continuum volumetric strains and continuum pressures. Element-wise total and continuum volumetric strains are defined as $\mathrm{E}_j^v = \mathrm{tr}(\mathbf{E}_j) = \Delta|\Omega_j^{\mathcal{D}}|/|\Omega_j^{\mathcal{D},0}|$ and $\mathrm{E}_{j,\alpha}^v = \Delta|\Omega_{j,\alpha}^{\mathcal{D}}|/|\Omega_{j,\alpha}^{\mathcal{D},0}|$, respectively. We compare averaged results over the FS with element-level results from the DC. To enable the former, we define the following discrete continuum counterpart to Equation (2):

$$\bar{z}_{j,\alpha}^{\mathcal{D}} = \frac{1}{|\Omega_{j,\alpha}^{\mathcal{D}}|}\int_{\Omega_{j,\alpha}^{\mathcal{D}}} z^h(\boldsymbol{x})\, dV, \tag{85}$$

where $z$ is a scalar field of interest. Continuum averaged pressures and volumetric strains can then be recovered using Equation (85) with discrete microscopic fields $p^h$ or $\epsilon^{v,h}$ in place of $z^h$. Total volumetric strain is likewise obtained using Equation (85) by replacing $|\Omega_{j,\alpha}^{\mathcal{D}}|$ with $|\Omega_j^{\mathcal{D}}|$.

For the DC problem, pressures and element-wise total volumetric strain are recovered naturally from the element centroid.[55] To get continuum strains, however, we must take a different approach. Starting with the matrix continuum, and comparing a volume averaged change in local porosity, Equation (4), to the effective change in matrix porosity given by Equation (41), such that $\mathrm{d}\phi_m = v_m \mathrm{d}\varphi_m$, allows us to derive the following expression for the volumetric matrix strain:

$$\mathrm{E}_m^v = \boldsymbol{1} : \bar{\boldsymbol{\epsilon}}_m = \frac{1}{b_m}\left[\frac{1}{v_m}\left(B_m \boldsymbol{1} : \mathbf{E} + \frac{P_m}{N_m} + \frac{P_f}{Q}\right) - \frac{P_m}{n_m}\right]. \tag{86}$$

We note that the expression for $\mathrm{E}_m^v$ in Equation (86) is only possible for an isotropic matrix as the inverse contraction map involving $\boldsymbol{b}_m$ is otherwise ill-posed. With $\mathrm{E}^v$ and $\mathrm{E}_m^v$, we can recover the fracture volumetric strain, $\mathrm{E}_f^v$, for the DC model using Equation (14).

## 4.3 | Results and discussion

Here, we present the results and analyses for the numerical test cases described in Section 4.1 under the modelling considerations described above. All results are given from observation points such as that shown in Figure 4.

### 4.3.1 | Undeformable isotropic

Figure 5 shows the element-averaged pressure evolutions from both FS explicit and DC simulations for the undeformable isotropic material case. Both models show a rapid decrease in fracture pressure within the first

millisecond followed by a delayed pressure response in the matrix. These general patterns can be attributed to the contrast in continuum permeabilities. Whilst both models show general decreasing trends, the FS fracture pressure decrease begins to smooth out at lower pressures. Further, the onset of FS matrix pressure diffusion happens earlier. When matrix pressure diffusion does occur in the DC model, the process occurs more rapidly (indicated by a steeper gradient) than in the FS case.

The disparities in matrix and fracture pressure diffusion between the two modelling approaches arise from the first-order transfer term, Equation (46), used by the DC model. In using a linear mass transfer model, one implicitly places a pseudosteady-state diffusion assumption on the communication between matrix and fracture continua. As a result, transient matrix drainage effects are neglected by the DC approach. Neglecting transient effects leads to the delay in DC matrix pressure diffusion we see in Figure 5, and the loss of pressure support in the fractures.

Shortcomings of using simplified transfer concepts have been well documented in literature (e.g., previous studies[67,68]). Previous works have thus sought to improve on the linear inter-continuum flow coupling term by including transient effects (other studies[3,69-71]). However, in the current work, we acknowledge the shortcomings of the transfer term used herein, with the focus being on understanding the coupled poroelastic behaviour.

### 4.3.2 | Deformable isotropic

Pressure and total element volumetric strain results for the deformable isotropic case are shown in Figure 6. In Figure 6A, both modelling approaches predict higher induced initial pressures in the fracture than in the matrix.

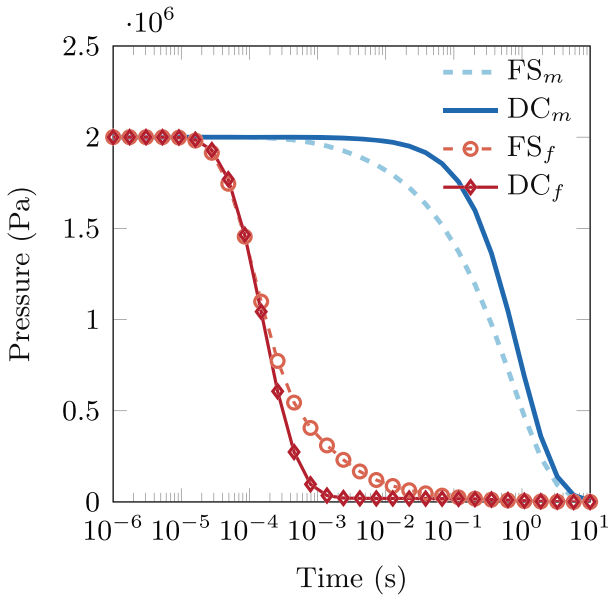


**FIGURE 5** Matrix and fracture continuum element averaged pressure evolutions for the undeformable isotropic test case. '$FS_\alpha$' and '$DC_\alpha$' denote quantities related to fine-scale and dual-continuum models for continuum $\alpha$, respectively [Colour figure can be viewed at wileyonlinelibrary.com]

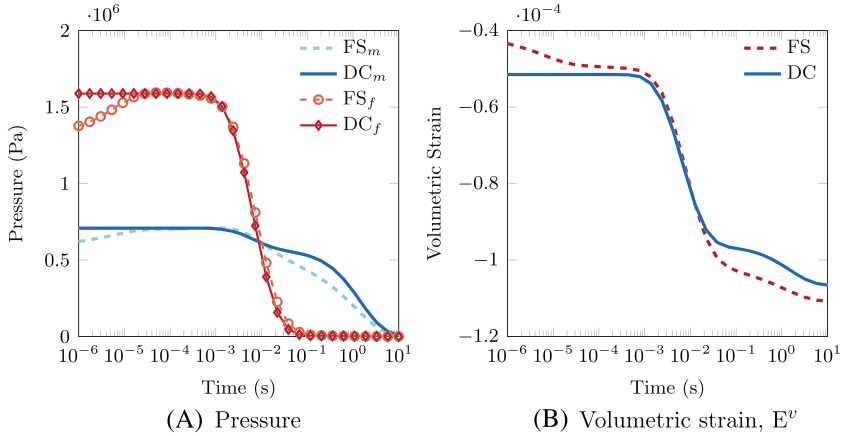


**FIGURE 6** (A) Matrix and fracture continuum element-averaged pressure and (B) total element volumetric strain evolutions for the deformable isotropic test case. '$FS_\alpha$' and '$DC_\alpha$' denote quantities related to fine-scale and dual-continuum models for continuum $\alpha$, respectively [Colour figure can be viewed at wileyonlinelibrary.com]

Further, both approaches show rapid decreases in fracture pressure and gradual decreases in matrix pressure. In Figure 6B, the FS and DC models show increasing volumetric strain evolution behaviours. However, for both pressure and strain, specific differences of the variable fields between the two modelling approaches may be observed at both early and late times. The disparity in late-time matrix pressure evolution (Figure 6A) is again due to the first-order intercontinuum transfer model (see Section 4.3.1). Over the same late-time period, we also observe a difference in volumetric strain (Figure 6B).

Of more interest in Figure 6 are the early-time results for continuum pressures. In Figure 6A, both FS matrix and fracture pressures exhibit nonmonotonic behaviour, known as the Mandel-Cryer effect. These pressure rises are not seen in the DC pressure responses. A similar observation was also made in the work of Zhang et al,[13] albeit for a different problem.

Figure 7 shows individual continuum volumetric strain evolutions. In Figure 7B, both modelling approaches show similar increasing strain behaviour with time. However, in Figure 7A, we observe that the FS matrix strain shows early-time nonmonotonic behaviour, contrary to DC matrix strain.

The early nonmonotonic differences in pressure and matrix strain between the two modelling approaches result from the underlying pressure assumption made for the DC model. In the derivation of the constitutive model in Section 2.2, we assumed a local equilibrium of pressure within each continuum over an REV. The induced response predicted in by the DC model is thus for a system in mechanical and hydrostatic equilibrium. Instead, the FS model makes no such pressure assumption. To understand the specific impacts of the latter, it is interesting to look at the local flow and deformation behaviours shown by the FS.

Figure 8 shows the FS pressure and volumetric strain responses within the first 100 μs. At $t_{0+}$ in Figure 8A, we observe pressure in the horizontal fracture is higher than the vertical fracture. This disequilibrium is concurrent with the negative and positive fracture strains for the horizontal and vertical fractures, respectively (Figure 8B). From $t_{0+}$ to $t_1$, Figure 8A shows that, away from the fracture intersection, horizontal fracture pressure drops slightly. However, vertical fracture pressure increases. These pressure changes occur with further contraction and expansion, respectively (Figure 8B). Over the same time period, matrix strain increases (Figure 8C). From $t_1$ to $t_5$, the pressure in both fractures is increasing (Figure 8A), with matrix and fracture deformations following the same evolution paths described previously. Finally, at $t_{10}$, the fractures reach a pressure equilibrium (Figure 8A).

We can now explain the early-time nonmonotonic behaviours in Figures 6A and 7A with the description of the local processes shown in Figure 8. Following $t_{0+}$, intrafracture flow is driven by the pressure disequilibrium between the horizontal and vertical fractures. Between $t_{0+}$ and $t_1$, horizontal fracture contraction occurs primarily due to the dissipation of the fluid pressure support. Vertical fracture expansion follows due to poroelastic coupling to accommodate incoming fluid from the horizontal fracture. As the vertical fracture expands, it forces the contraction of the matrix, and thus the increasing matrix strain shown in Figures 7A and 8. After $t_1$, deformation drives the horizontal fracture pressure increase due to fluid compressibility. The overall fracture continuum pressure increases (Figure 6A), with strain generating pressure in the horizontal fracture whilst the pressure change associated with vertical fracture expansion slows. The latter occurs due to the low matrix permeability which prohibits dissipation of excess matrix pressure, until later times. As a result, the undrained matrix stiffness increases with its progressive contraction, slowing vertical fracture

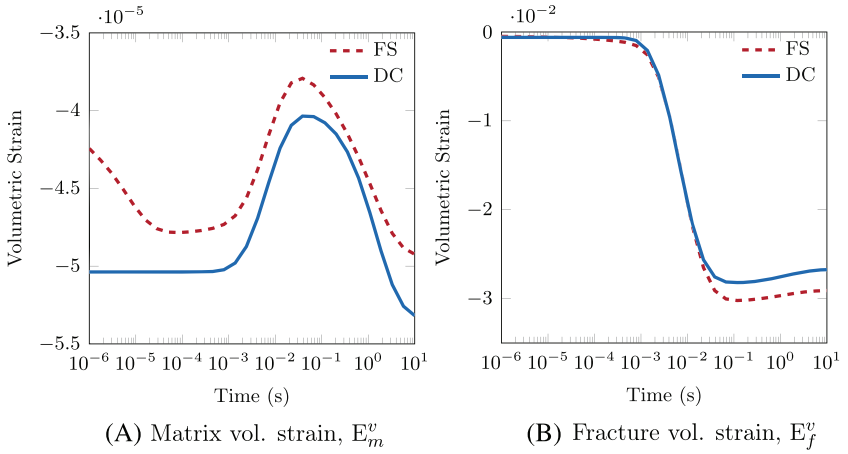


(A) Matrix vol. strain, $E_m^v$ (B) Fracture vol. strain, $E_f^v$

**FIGURE 7** (A) Matrix and (B) fracture volumetric strain evolutions for the deformable isotropic test case. 'FS' and 'DC' denote quantities related to fine-scale and dual-continuum models [Colour figure can be viewed at wileyonlinelibrary.com]

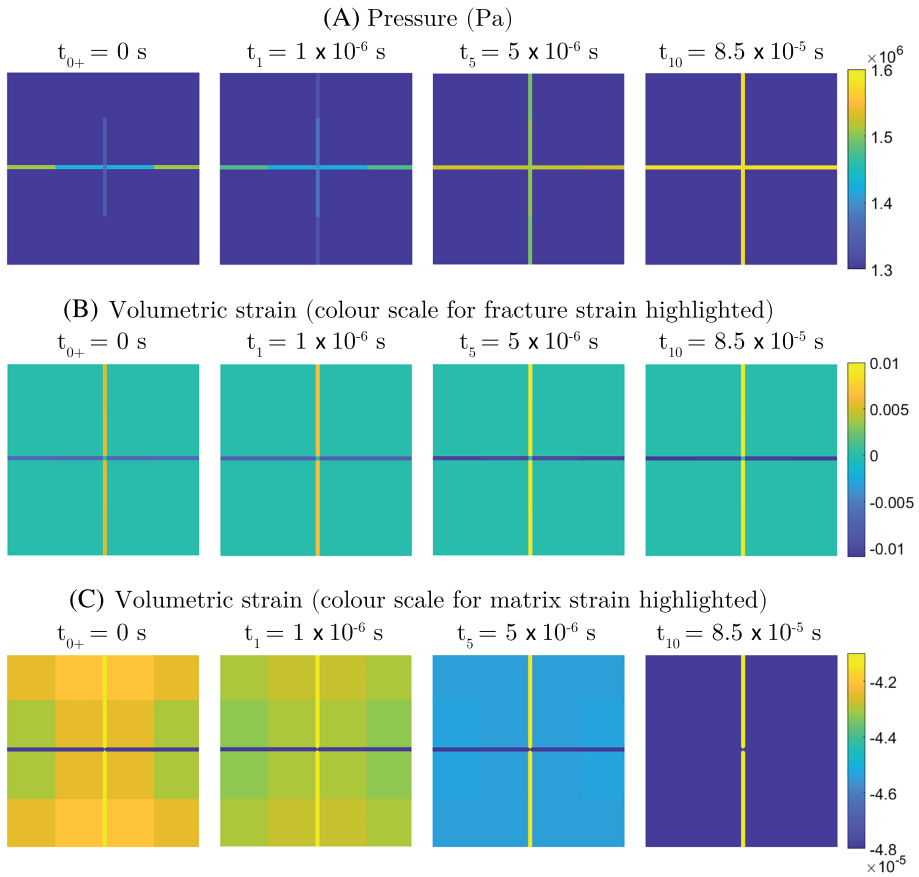


**FIGURE 8** (A) Pressure and volumetric strain (highlighted for fractures and matrix, (B) and (C), respectively) fields at different time levels, $t_i$, for the fine-scale (FS) representation of the deformable isotropic material. Each field plot is 5 mm × 5 mm and is located at the observation point. Subscript 0+ denotes the time level corresponding to the undrained, loaded configuration [Colour figure can be viewed at wileyonlinelibrary.com]

expansion until a mechanical equilibrium is reached. The overall fracture continuum pressure rise finally stops when the fractures have reached mechanical equilibrium with the matrix and an internal hydrostatic equilibrium.

The local processes shown by the FS model are not captured by the DC model due to the underlying homogenisation assumptions made in the latter. However, Figures 6 and 7 do show that, aside from the local equilibration processes, the DC model can capture the global poroelastic behaviours of the FS model.

### 4.3.3 | Geometry-induced anisotropy: Explicit computation of $\mathbb{C}^*$

Here, we show the results for the geometry-induced (single-fracture set) anisotropy case. Pressure and total volumetric strain are given in Figure 9, whilst Figure 10 shows the individual continuum volumetric strains.

Figure 9A now shows a smaller disparity between the initial matrix and fracture pressures, with the fracture pressure being only slightly higher. Further, we do not observe the Mandel-Cryer effect in the FS model. However, away from the initial pressures, the general trends we see in Figure 6A can still be observed in Figure 9A. Specifically, a rapid decrease in fracture pressure is followed by a smoother matrix pressure decrease. As expected, the late-time differences in matrix pressure observed previously are present in the current test. For both modelling approaches, there is a good agreement in matrix and fracture pressure evolutions. The total element volumetric strain evolutions are also similar between the two modelling approaches, with an overall increase in strain as the material compacts.

The similarity in total volumetric strain between the two approaches is reflected in the individual continuum strains (Figure 10). The matrix shows early-time expansion behaviour followed by contraction. Fracture deformation is coupled to matrix deformation (and vice versa). Fracture contraction is therefore followed by a period of expansion as the matrix drains and contracts.

The small difference in initial continuum pressures observed in Figure 9A can be explained by considering the geometric anisotropy induced by the fractures. With the fracture set being aligned with the direction of loading (Figure 3A), the stiffer matrix acts like a series of columns, supporting a significant portion of the applied load. Through the coupling between stress and pressure, the low portion of stress 'seen' by the fracture phase leads to the low induced

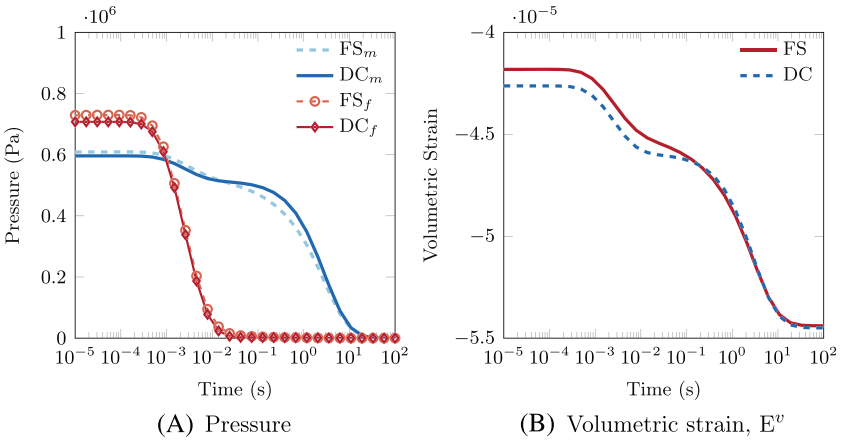


**FIGURE 9** (A) Matrix and fracture continuum element averaged pressure and (B) total element volumetric strain evolutions for the (deformable) anisotropic test case with one (vertical) fracture set. '$FS_\alpha$' and '$DC_\alpha$' denote quantities related to fine-scale and dual-continuum models for continuum $\alpha$, respectively [Colour figure can be viewed at wileyonlinelibrary.com]

(A) Pressure (B) Volumetric strain, $E^v$

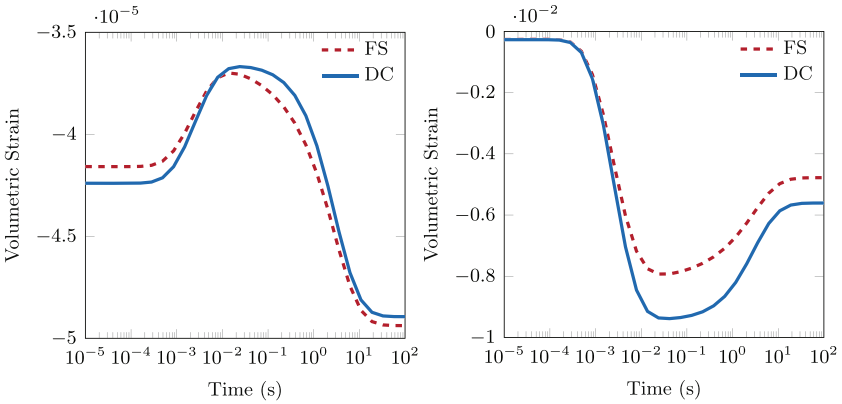


**FIGURE 10** (A) Matrix and (B) fracture volumetric strain evolutions for the (deformable) anisotropic test case with one (vertical) fracture set. 'FS' and 'DC' denote quantities related to fine-scale and dual-continuum models [Colour figure can be viewed at wileyonlinelibrary.com]

(A) Matrix vol. strain, $E^v_m$ (B) Fracture vol. strain, $E^v_f$

fracture pressure shown in Figure 9A. Finally, the absence of the Mandel-Cryer effect in the current case is due to the pressure being at equilibrium within the single fracture set. As a result, local processes do not drive early-time poroelastic intracontinuum and intercontinuum pressure generation.

### 4.3.4 | Material-induced anisotropy: Numerical computation of $\mathbb{C}^*$

Figures 11 and 12 show pressure and total strain and individual continuum strain results, respectively, for the material-induced anisotropy case. Both models in Figure 11A show a strong difference in the early-time magnitudes of matrix and fracture pressures. The FS model shows similar early-time Mandel-Cryer fracture behaviour to what we observed in Figure 6A. In contrast, the FS matrix nonmonotinicity is negligible in Figure 11A compared with the isotropic case. At later times, we see a significant nonmontonic evolution in matrix pressure that is shown by *both* modelling approaches. This nonmonotonic matrix pressure rise starts earlier in the FS model than the DC model. Finally, we observe that matrix and fracture diffusion starts at similar times, indicating a single-continuum response. Coupled to the delayed fracture diffusion response is the delayed increase in total volumetric strain (Figure 11B).

In Figure 12, both modelling approaches give similar continuum strain evolutions. Similar to Figure 7A, Figure 12A shows that the DC approach misses the early-time matrix strain nonmonotinicity displayed by the FS approach. However, contrast to Figure 7A, Figure 12A shows a smoother early-time FS matrix strain nonmonotinicity, whilst the late-time matrix strain nonmonotinicity for both approaches is much sharper.

Results in Figures 11 and 12 can be explained by considering the material anisotropy in the fracture continuum. The smoother early-time nonmonotinicity in FS matrix strain occurs because the vertical fractures are stiffer. These fractures then expand less with incoming fluid, reducing poroelastic coupling (and thus deformation) with the matrix compared with the isotropic case. As a result, since FS matrix pressure does not change significantly, the initial matrix

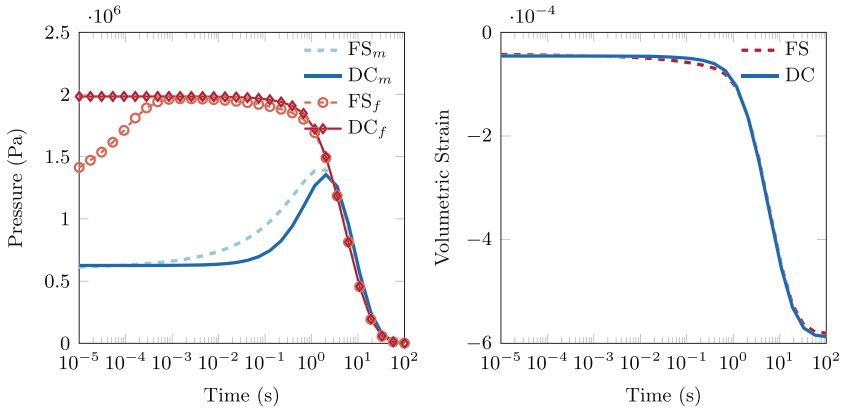


(A) Pressure (B) Volumetric strain, $E^v$

**FIGURE 11** (A) Matrix and fracture continuum element averaged pressure and (B) total element volumetric strain evolutions for the (deformable) anisotropic test case with two orthogonal fracture sets. '$FS_\alpha$' and '$DC_\alpha$' denote quantities related to fine-scale and dual-continuum models for continuum $\alpha$, respectively [Colour figure can be viewed at wileyonlinelibrary.com]

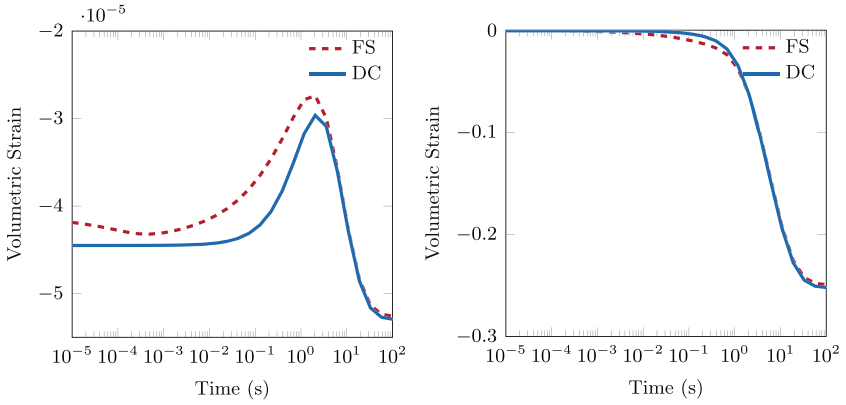


(A) Matrix vol. strain, $E^v_m$ (B) Fracture vol. strain, $E^v_f$

**FIGURE 12** (A) Matrix and (B) fracture volumetric strain evolutions for the (deformable) anisotropic test case with two orthogonal fracture sets. 'FS' and 'DC' denote quantities related to fine-scale and dual-continuum models [Colour figure can be viewed at wileyonlinelibrary.com]

pressures for the two modelling approaches are similar. This result suggests that mechanical anisotropy can noticeably affect the degree of intercontinuum coupling. The delay in fracture pressure diffusion occurs due to the low vertical fracture permeability. Accordingly, we see the nonmonotonic rise in matrix pressure with local intercontinuum equilibration processes occuring at similar timescales to macroscopic fracture flow. Further, the pseudosteady-state mass transfer assumption leads to the delayed response of this nonmonotinicity in the DC model. The influx of fluid from the fractures into the matrix is accompanied by expansion of the matrix material, followed by contraction as fluid drains out (Figure 12A).

The results in the current test show again how the DC model misses early-time effects due to local equilibration processes. Neglecting these local processes is implicit due to the steady-state pressure assumption made during homogenisation. However, once local equilibration is reached, the DC model does predict the general poroleastic behaviours of the FS model.

## 5 | CONCLUSIONS

DC models are an implicit approach to modelling multiscale materials. Further, with the appropriate extensions, they can be used to model complex multiphysics problems such as the coupled mechanics and flow phenomena studied in this work.

In this paper, we derived a DC poroelastic constitutive model that makes no assumptions on the material symmetry and mechanical properties of the dual-material and its constituents. We termed the resulting model the anisotropic, dual-stiffness constitutive model. Further, we discussed how under isotropy of the continua and bulk material, and void space assumptions of the high-permeability transport phase, previously introduced constitutive models can be recovered from the constitutive model developed herein.

Second, using numerical modelling, we investigated whether the DC approach with the derived constitutive model is able to capture the global poroelastic behaviours of FS explicit models. We introduced the computational framework used to carry out our investigation and described the resulting numerical tests therein. We observed that anisotropy can have measurable impacts on flow and deformation behaviour. However, we showed that the DC approach is capable of capturing the global poroelastic behaviours for both isotropic and anisotropic FS equivalents. Discrepancies between the two model representations arise when local equilibration processes not accounted for in the homogenisation approach are significant.

Finally, interesting extensions to the current work involve the study of nonlinear poromechanical effects and measurement methodologies for the material parameters used herein. In the former, it is well known that fracture (and soil aggregate) deformation is geometrically nonlinear, leading to coupled material nonlinearities at the macroscopic scale. Modelling these scale effects requires comprehensive multiscale modelling approaches and is an active area of research.[25,72,73] Lastly, in analogy to the work of Biot and Willis,[74] it is highly desirable to develop methods of measurement for the parameters introduced in this work. In particular, the challenge remains on how to map individual fracture characteristics to continuum properties. In this context, a microporomechanics framework could provide useful insights into experimental and theoretical methodologies (e.g., Lemarchand et al[15]).

## ACKNOWLEDGEMENTS

The authors are very grateful for the funding provided to them by the Natural Environmental Research Council to carry out this work and to the reviewers who have helped to improve it.

## ORCID

*Mark Ashworth* https://orcid.org/0000-0003-2933-6010

## REFERENCES

1. Barenblatt G, Zheltov I, Kochina I. Basic concepts in the theory of seepage of homogeneous liquids in fissured rocks [strata]. *J Appl Math Mech*. 1960;24(5):1286-1303.
2. Gerke HH, Van Genuchten MT. A dual-porosity model for simulating the preferential movement of water and solutes in structured porous media. *Water Res Res*. 1993;29(2):305-319.
3. March R, Doster F, Geiger S. Accurate early-time and late-time modeling of countercurrent spontaneous imbibition. *Water Res Res*. 2016;52(8):6263-6276.
4. Reimus P, Pohll G, Mihevc T, et al. Testing and parameterizing a conceptual model for solute transport in a fractured granite using multiple tracers in a forced-gradient test. *Water Res Res*. 2003;39(12):1356–1370.
5. Wu Y-S, Zhang W, Pan L, Hinds J, Bodvarsson G. Modeling capillary barriers in unsaturated fractured rock. *Water Res Res*. 2002;38(11):35–1-35–12.
6. Berryman JG, Wang HF. The elastic coefficients of double-porosity models for fluid transport in jointed rock. *J Geophys Res Solid Earth*. 1995;100(B12):24611-24627.
7. Choo J, Borja RI. Stabilized mixed finite elements for deformable porous media with double porosity. *Comput Methods Appl Mech Eng*. 2015;293:131-154.
8. Khalili N, Valliappan S. Unified theory of flow and deformantion in double porous media. *Eur J Mech A Solids*. 1996;15(2):321-336.
9. Loret B, Rizzi E. Strain localization in fluid-saturated anisotropic elastic-plastic porous media with double porosity. *J Mech Phys Solids*. 1999;47(3):503-530.
10. Babuska V, Cara M. *Seismic Anisotropy in the Earth, Vol. 10*. Dordrecht, Netherlands: Springer Science & Business Media; 1991.
11. Price NJ, Cosgrove JW. *Analysis of Geological Structures*. New York, USA: Cambridge University Press; 1990.
12. Snow DT. Anisotropic permeability of fractured media. *Water Res Res*. 1969;5(6):1273-1289.
13. Zhang Q, Choo J, Borja RI. On the preferential flow patterns induced by transverse isotropy and non-Darcy flow in double porosity media. *Comput Methods Appl Mech Eng*. 2019;353:570–592.
14. Jaeger JC, Cook NG, Zimmerman R. *Fundamentals of Rock Mechanics*. Oxford, UK: John Wiley & Sons; 2009.
15. Lemarchand E, Davy CA, Dormieux L, Chen W, Skoczylas F. Micromechanics contribution to coupled transport and mechanical properties of fractured geomaterials. *Transp Porous Media*. 2009;79(3):335-358.
16. Olsson R, Barton N. An improved model for hydromechanical coupling during shearing of rock joints. *Int J Rock Mech Mining Sci*. 2001;38(3):317-329.
17. Berryman JG. Extension of poroelastic analysis to double-porosity materials: new technique in microgeomechanics. *J Eng Mech*. 2002;128(8):840-847.
18. Berryman JG, Pride SR. Models for computing geomechanical constants of double-porosity materials from the constituents' properties. *J Geophys Res Solid Earth*. 2002;107(B3):ECV-2.
19. Elsworth D, Bai M. Flow-deformation response of dual-porosity media. *J Geotech Eng*. 1992;118(1):107-124.

20. Nguyen VX, Abousleiman YN. Poromechanics solutions to plane strain and axisymmetric Mandel-type problems in dual-porosity and dual-permeability medium. *J Appl Mech*. 2010;77(1):11002–1-11002–18.
21. Dormieux L, Kondo D, Ulm F-J. *Microporomechanics*. Chichester, UK: John Wiley & Sons; 2006.
22. Ashworth M, Doster F. Foundations and their practical implications for the constitutive coefficients of poromechanical dual-continuum models. *Trans Porous Med*. 2019b;130(3):699-730.
23. Egya DO, Geiger S, Corbett PWM, et al. Analysing the limitations of the dual-porosity response during well tests in naturally fractured reservoirs. *Petroleum Geosci*. 2019;25(1):30-49.
24. Lewandowska J, Szymkiewicz A, Burzyński K, Vauclin M. Modeling of unsaturated water flow in double-porosity soils by the homogenization approach. *Adv Water Res*. 2004;27(3):283-296.
25. Borja RI, Choo J. Cam-clay plasticity, part VIII: a constitutive framework for porous materials with evolving internal structure. *Comput Methods Appl Mech Eng*. 2016;309:653-679.
26. Bemer E, Boutéca M, Vincké O, Hoteit N, Ozanam O. Poromechanics: from linear to nonlinear poroelasticity and poroviscoelasticity. *Oil Gas Sci Technol*. 2001;56(6):531-544.
27. Bidgoli MN, Zhao Z, Jing L. Numerical evaluation of strength and deformability of fractured rocks. *J Rock Mech Geotech Eng*. 2013;5(6):419-430.
28. Deude V, Dormieux L, Kondo D, Maghous S. Micromechanical approach to nonlinear poroelasticity: application to cracked rocks. *J Eng Mech*. 2002;128(8):848-855.
29. Choo J, White JA, Borja RI. Hydromechanical modeling of unsaturated flow in double porosity media. *Int J Geomech*. 2016;16(6):D4016002.
30. Bear J, Bachmat Y. *Introduction to Modeling of Transport Phenomena in Porous Media, Vol. 4*. Dordrecht, Netherlands: Springer Science & Business Media; 2012.
31. Auriault J-L. Upscaling heterogeneous media by asymptotic expansions. *J Eng Mech*. 2002;128(8):817-822.
32. Geers MG, Kouznetsova VG, Brekelmans W. Multi-scale computational homogenization: trends and challenges. *J Comput Appl Math*. 2010;234(7):2175-2182.
33. Berre I, Doster F, Keilegavlen E. Flow in fractured porous media: a review of conceptual models and discretization approaches. *Transp Porous Media*. 2019;130(1):215-236.
34. Long J, Remer J, Wilson C, Witherspoon P. Porous media equivalents for networks of discontinuous fractures. *Water Res Res*. 1982;18(3):645-658.
35. Min K-B, Jing L. Numerical determination of the equivalent elastic compliance tensor for fractured rock masses using the distinct element method. *Int J Rock Mech Mining Sci*. 2003;40(6):795-816.
36. Neuman SP. Stochastic continuum representation of fractured rock permeability as an alternative to the rev and fracture network concepts. *Groundwater Flow and Quality Modelling*. Dordrecht, Netherlands: Springer; 1988:331-362.
37. Berkowitz B. Characterizing flow and transport in fractured geological media: a review. *Adv Water Res*. 2002;25(8-12):861-884.
38. Nemat-Nasser S, Hori M. *Micromechanics: Overall Properties of Heterogeneous Materials*. Amsterdam, Netherlands: Elsevier; 1993.
39. Biot MA. General theory of three-dimensional consolidation. *J Appl Phys*. 1941;12(2):155-164.
40. Coussy O. *Poromechanics*. Chichester, UK: John Wiley & Sons; 2004.
41. Van den Eijnden A, Bésuelle P, Chambon R, Collin F. A FE2 modelling approach to hydromechanical coupling in cracking-induced localization problems. *Int J Solids Struct*. 2016;97:475-488.
42. Chateau X, Dormieux L. Micromechanics of saturated and unsaturated porous media. *Int J Numer Anal Methods Geomech*. 2002;26(8):831-844.
43. Hashin Z. Theory of fiber reinforced materials. NASA CR-1974; 1972.
44. Hill R. Elastic properties of reinforced solids: Some theoretical principles. *J Mech Phys Solids*. 1963;11(5):357-372.
45. Levin V. On the coefficients of thermal expansion of heterogeneous materials. *Mech Solids*. 1967;2:58-61.
46. Borja RI, Koliji A. On the effective stress in unsaturated porous continua with double porosity. *J Mech Phys Solids*. 2009;57(8):1182-1193.
47. Koliji A, Vulliet L, Laloui L. New basis for the constitutive modelling of aggregated soils. *Acta Geotech*. 2008;3(1):61.
48. Kim J, Sonnenthal EL, Rutqvist J. Formulation and sequential numerical algorithms of coupled fluid/heat flow and geomechanics for multiple porosity materials. *Int J Numer Methods Eng*. 2012;92(5):425-456.
49. Warren JE, Root PJ. The behavior of naturally fractured reservoirs. *Soc Petroleum Eng J*. 1963;3(03):245-255.
50. Lim KT, Aziz K. Matrix-fracture transfer shape factors for dual-porosity simulators. *J Petrol Sci Eng*. 1995;13(3-4):169-178.
51. Beirão da Veiga L, Brezzi F, Cangiani A, Manzini G, Marini LD, Russo A. Basic principles of virtual element methods. *Math Models Methods Appl Sci*. 2013;23(01):199-214.
52. Gain AL, Talischi C, Paulino GH. On the virtual element method for three-dimensional linear elasticity problems on arbitrary polyhedral meshes. *Comput Methods Appl Mech Eng*. 2014;282:132-160.
53. Lie K-A. *An Introduction to Reservoir Simulation Using MATLAB/GNU Octave*. Cambridge, UK: Cambridge University Press; 2019.
54. Lie K-A, Krogstad S, Ligaarden IS, Natvig JR, Nilsen HM, Skaflestad B. Open-source MATLAB implementation of consistent discretisations on complex grids. *Comput Geosci*. 2012;16(2):297-322.
55. Andersen O, Nilsen HM, Raynaud X. Coupled geomechanics and flow simulation on corner-point and polyhedral grids. In: *SPE Reservoir Simulation Conference Society of Petroleum Engineers*. Montgomery, Texas, USA; 2017a.

56. Andersen O, Nilsen HM, Raynaud X. Virtual element method for geomechanical simulations of reservoir models. *Comput Geosci*. 2017b; 21(5-6):877-893.
57. Ashworth M, Doster F. An open source numerical framework for dual-continuum geomechanical simulation. In: *SPE Reservoir Simulation Conference Society of Petroleum Engineers*. Galveston, Texas, USA; 2019a.
58. Coulet J, Faille I, Girault V, Guy N, Nataf F. A fully coupled scheme using virtual element method and finite volume for poroelasticity. *Comput Geosci*. 2019;24:1-23.
59. Da Veiga LB, Lovadina C, Mora D. A virtual element method for elastic and inelastic problems on polytope meshes. *Comput Methods Appl Mech Eng*. 2015;295:327-346.
60. Lewis RW, Schrefler BA. *The Finite Element Method in the Static and Dynamic Deformation and Consolidation of Porous Media*. Chichester, UK: John Wiley & Sons; 1998.
61. Witherspoon PA, Wang JS, Iwai K, Gale JE. Validity of cubic law for fluid flow in a deformable rock fracture. *Water Res Res*. 1980;16(6): 1016-1024.
62. Hashin Z, Shtrikman S. A variational approach to the theory of the elastic behaviour of multiphase materials. *J Mech Phys Solids*. 1963; 11(2):127-140.
63. Torquato S. *Random Heterogeneous Materials: Microstructure and Macroscopic Properties*. New York, USA: Springer; 2002.
64. Daniel IM, Ishai O, Daniel IM, Daniel I. *Engineering Mechanics of Composite Materials, Vol. 3*. New York: Oxford university press; 1994.
65. Pecullan S, Gibiansky L, Torquato S. Scale effects on the elastic behavior of periodic andhierarchical two-dimensional composites. *J Mech Phys Solids*. 1999;47(7):1509-1542.
66. Royer P, Auriault J-L, Lewandowska J, Serres C. Continuum modelling of contaminant transport in fractured porous media. *Transp Porous Media*. 2002;49(3):333-359.
67. Berkowitz B, Bear J, Braester C. Continuum models for contaminant transport in fractured porous formations. *Water Res Res*. 1988;24 (8):1225-1236.
68. Lemonnier P, Bourbiaux B. Simulation of naturally fractured reservoirs. State of the art-part 2-matrix-fracture transfers and typical features of numerical studies. *Oil Gas Sci Technol Revue de l'Inst Français du Pétrole*. 2010;65(2):263-286.
69. Sarma P, Aziz K. New Transfer Functions for Simulation of Naturally Fractured Reservoirs with Dual Porosity Models. *SPE Annual Technical Conference and Exhibition*; Society of Petroleum Engineers. Houston, Texas, USA; 2004.
70. Zhou Q, Oldenburg CM, Spangler LH, Birkholzer JT. Approximate solutions for diffusive fracture-matrix transfer: application to storage of dissolved co2 in fractured rocks. *Water Res Res*. 2017;53(2):1746-1762.
71. Zimmerman RW, Chen G, Hadgu T, Bodvarsson GS. A numerical dual-porosity model with semianalytical treatment of fracture/matrix flow. *Water Res Res*. 1993;29(7):2127-2137.
72. Castelletto N, Klevtsov S, Hajibeygi H, Tchelepi HA. Multiscale two-stage solver for Biot's poroelasticity equations in subsurface media. *Comput Geosci*. 2019;23(2):207-224.
73. Wang K, Sun W. A multiscale multi-permeability poroplasticity model linked by recursive homogenizations and deep learning. *Comput Methods Appl Mech Eng*. 2018;334:337-380.
74. Biot MA, Willis D. The elastic coefficients of the theory of consolidation. *J Appl Mech*. 1957;15:594-601.


**How to cite this article:** Ashworth M, Doster F. Anisotropic dual-continuum representations for multiscale poroelastic materials: Development and numerical modelling. *Int J Numer Anal Methods Geomech*. 2020;1–25. https://doi.org/10.1002/nag.3140